

RESEARCH ARTICLE

Adenine nucleotide translocase regulates airway epithelial metabolism, surface hydration and ciliary function

Corrine R. Kliment^{1,2,3,*}, Jennifer M. K. Nguyen^{2,4}, Mary Jane Kaltreider³, YaWen Lu⁵, Steven M. Claypool⁵, Josiah E. Radder³, Frank C. Sciurba³, Yingze Zhang³, Alyssa D. Gregory³, Pablo A. Iglesias⁶, Venkataramana K. Sidhaye^{2,7} and Douglas N. Robinson^{1,2,4,8,*}

ABSTRACT

Airway hydration and ciliary function are critical to airway homeostasis and dysregulated in chronic obstructive pulmonary disease (COPD), which is impacted by cigarette smoking and has no therapeutic options. We utilized a high-copy cDNA library genetic selection approach in the amoeba *Dictyostelium discoideum* to identify genetic protectors to cigarette smoke. Members of the mitochondrial ADP/ATP transporter family adenine nucleotide translocase (ANT) are protective against cigarette smoke in *Dictyostelium* and human bronchial epithelial cells. Gene expression of ANT2 is reduced in lung tissue from COPD patients and in a mouse smoking model, and overexpression of ANT1 and ANT2 resulted in enhanced oxidative respiration and ATP flux. In addition to the presence of ANT proteins in the mitochondria, they reside at the plasma membrane in airway epithelial cells and regulate airway homeostasis. ANT2 overexpression stimulates airway surface hydration by ATP and maintains ciliary beating after exposure to cigarette smoke, both of which are key functions of the airway. Our study highlights a potential for upregulation of ANT proteins and/or of their agonists in the protection from dysfunctional mitochondrial metabolism, airway hydration and ciliary motility in COPD.

This article has an associated First Person interview with the first author of the paper.

KEY WORDS: Adenine nucleotide translocase, Airway epithelium, Cigarette smoke, Mitochondria, SLC25A4, SLC25A5

INTRODUCTION

Central to the function of human airway is the ability to maintain a surface hydration layer that allows the cilia to beat rhythmically to clear mucus, particulates, and infectious organisms from the airway passages. When homeostasis of airway hydration and ciliary

function are lost, lung diseases such as chronic obstructive pulmonary disease (COPD) develop (Wiegman et al. 2015). COPD is highly prevalent worldwide, comprising airspace enlargement and airway remodeling that lead to significant airflow limitations in patients (Vestbo et al., 2013). COPD increases morbidity and mortality and, as of January 2020 was the 4th leading cause of death in the United States, according to the Centers for Disease Control and Prevention (CDC) (Murphy et al., 2018), with cigarette smoke being a major inciting factor. Cigarette smoke exposure leads to cellular dysfunction, including changes in mitochondrial metabolism (Hoffmann et al., 2013; Wiegman et al., 2015) and abnormal function of ciliated airway cells (Astrand et al., 2015; Ghosh et al., 2015). Despite significant research in COPD pathogenesis, no effective therapies have yet been identified that prevent or reverse COPD development. Discovery-based studies in search of unrealized, essential biology are difficult to conduct in the complex tissue of the human lung.

In the search of new opportunities for addressing COPD pathogenesis, we leveraged the social amoeba *Dictyostelium discoideum* to identify genetic protectors from cigarette smoke. We used an expression cDNA library suppression approach with follow-up in primary human airway epithelial cells. We discovered that overexpression of canonical inner mitochondrial membrane transport proteins, i.e. of solute carrier family 25 members (SLC25As, also known as adenine nucleotide translocase ANT)s enhances mitochondrial metabolism and provides protection against cigarette smoke exposure. This finding is important as mitochondrial dysfunction has been linked to airway remodeling in COPD (Wiegman et al., 2015). There are four ANT paralogs in human – i.e. ANT1, ANT 2, ANT 3 and ANT 4 (officially known as SLC25A3, SLC25A5, SLC25A6 and SLC25A31, respectively), with ANT1–3 being present in the lung (data not shown) – which are known to regulate mitochondrial metabolism and cell fate, including senescence (Kretova et al., 2014) and mitophagy (Hoshino et al., 2019). In other disease scenarios, ANT1 deficiency results in hypertrophic cardiomyopathy, myopathy and lactic acidosis (Graham et al., 1997), whereas increases in ANT1 levels protect against cardiac ischemia (Klumpe et al., 2016; Lynn et al., 2010; Winter et al., 2016) and hepatotoxicity (Kim et al., 2012). Reduction in levels of ANT2 also protects adipocytes from hypoxia and inflammation (Seo et al., 2019) while leading to cardiomyocyte developmental abnormalities (Kokoszka et al., 2016).

Moreover, we found that ANT2 also plays an important role in airway epithelial biology, notably airway hydration, which promotes ciliary function. In COPD, the airway surface liquid (ASL) layer becomes dehydrated and ciliary movement is reduced (Astrand et al., 2015; Ghosh et al., 2015), contributing to abnormal muco-ciliary clearance. We found that ANT proteins are distributed

¹Department of Cell Biology, Johns Hopkins University School of Medicine, Baltimore, MD 21205, USA. ²Department of Medicine, Division of Pulmonary and Critical Care, Johns Hopkins University School of Medicine, Baltimore, MD 21205, USA. ³Department of Medicine, Division of Pulmonary and Critical Care, University of Pittsburgh, Pittsburgh, PA 15260, USA. ⁴Department of Pharmacology and Molecular Sciences, Johns Hopkins University School of Medicine, Baltimore, MD 21205, USA. ⁵Department of Physiology, Johns Hopkins University School of Medicine, Baltimore, MD 21205, USA. ⁶Department of Electrical and Computer Engineering, Johns Hopkins University, Baltimore, MD 21218, USA. ⁷Department of Environmental Health Sciences and Engineering, Johns Hopkins University School of Public Health, Baltimore, MD 21205, USA. ⁸Chemical and Biomolecular Engineering, Johns Hopkins University, Baltimore, MD 21218, USA.

*Authors for correspondence (ckliment@pitt.edu; dnr@jhmi.edu)

ORCID: C.R.K., 0000-0002-3815-9370; M.J.K., 0000-0003-2868-2050; Y.W.L., 0000-0003-0479-1471; V.K.S., 0000-0002-4506-8549; D.N.R., 0000-0003-1236-4891

Handling Editor: David Stephens

Received 12 November 2020; Accepted 13 January 2021

at the apical plasma membrane of airway epithelial cells. Moreover, we found that ANT2, in particular, interacts with the chemiosmotic circuit that controls airway hydration, facilitating robust ciliary beating.

RESULTS

Adenine nucleotide translocase identified as a genetic protector from cigarette smoke

Cigarette smoke is a primary insult that leads to the development of COPD and airway dysfunction. To identify potential genetic protectors against cigarette smoke, we utilized the model organism *Dictyostelium* as a tool to identify genes that could then be directly studied in human and mouse models of lung disease (Fig. 1A). We challenged cDNA library-transformed *Dictyostelium* cells – an expression cDNA library built from vegetative (growth phase) *Dictyostelium* cells (Robinson and Spudich, 2000; Zhou et al., 2010) – with cigarette smoke extract (CSE; prepared in *Dictyostelium* growth medium) at the EC40 concentration (the CSE concentration resulting in a 40% decrease in growth rate) (Fig. S1A, B). Over the course of ~3 weeks, we selected for ‘winning cells’ that were able to grow in the presence of CSE, with growth rates comparable to or exceeding that of untreated wild-type cells. We then isolated the plasmids from the winner cells and reintroduced them into fresh *Dictyostelium* cells to confirm the suppression

effects. From this, we identified the following genes in *Dictyostelium* as protectors against 40% cigarette smoke extract: adenine nucleotide translocase (ANT; encoded by *ancA*; Fig. 1B), actin-interacting protein-1 (AIP1; encoded by *aip1*), heat shock protein-70 (hsp70; encoded by *mhsp70*), and polyadenylate-binding protein 1A (PABP1; encoded by *pabpc1A*). Because the *ancA* plasmid was the strongest protector, ANT became the focus of this study. The recovered ANT cDNA lacked the initial 46 base pairs encoding the N-terminal amino acids of the first transmembrane span. Expression of full-length *ancA* gene in *Dictyostelium* also offered protection from 40% CSE (Fig. 1C). Adenine nucleotide translocase is an ADP/ATP transporter in the inner mitochondrial membrane. The human genome encodes four paralogs (ANT1-4), with variable tissue expression (Liu and Chen, 2013). ANT1, ANT2 and ANT3 paralogs are expressed in normal human bronchial epithelial cells with ANT2 being predominant (Fig. S1C). ANT proteins have 71–89% similarity between human isoforms and 62–68% similarity to *AncA* in *Dictyostelium* (Fig. S1D). We tested ANT1 and ANT2, and found that, overexpression of human ANT1 or ANT2 protect human bronchial epithelial cells (HBEC3-KTs) from cigarette smoke-induced cell death (Fig. 1D; see also Fig. S1E, F, adenovirus overexpression), after exposure to 10–80% of CSE. ANT1 overexpression alone may result in a slight increase in baseline growth rate in HBEC3-KTs. ANT overexpression does not

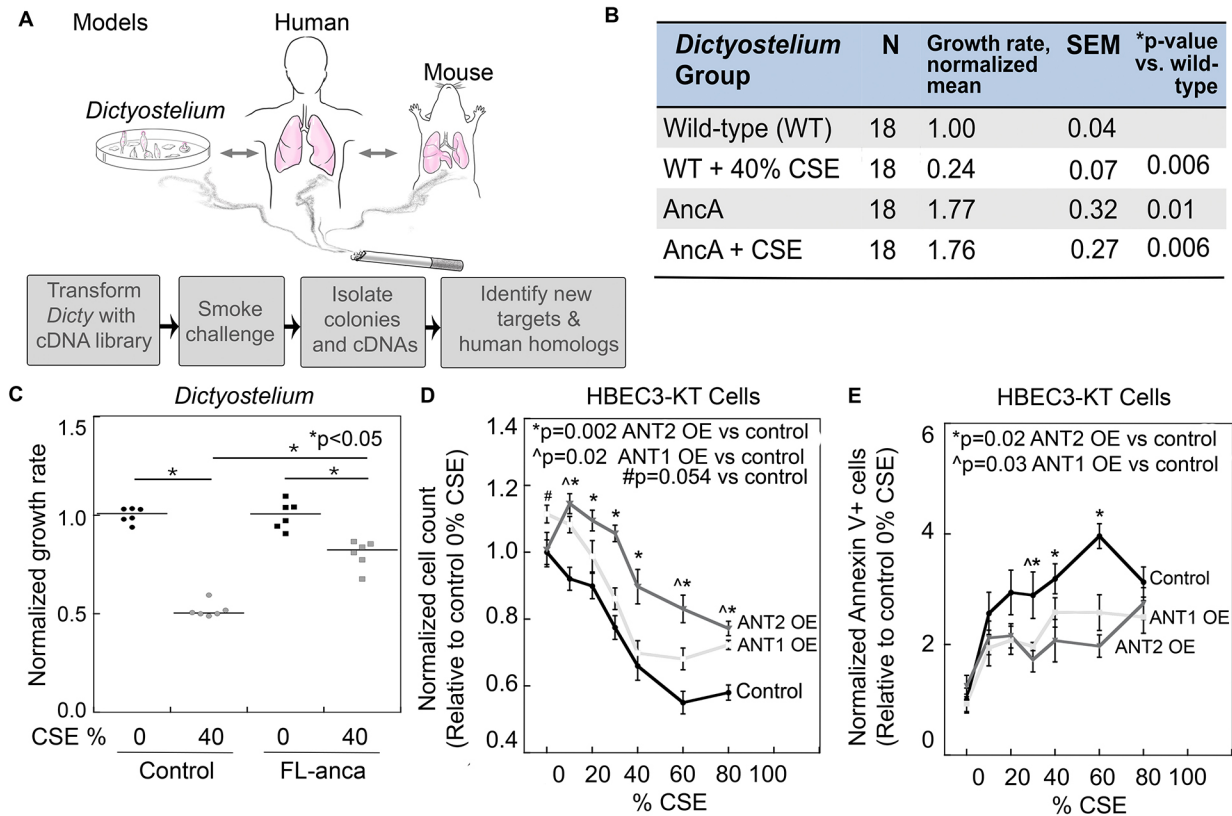


Fig. 1. ANT protects against cigarette smoke-induced cell death. (A) Models and experimental design leveraging *Dictyostelium* to identify relevant pathways in more-complex mammalian systems. (B) *Dictyostelium* high copy cDNA library suppression yielded ANT (encoded by the *ancA* gene; the initial cDNA plasmid clone had a small 46-bp deletion at the 5' end) as a strong protector against CSE. Introduction of the recovered plasmid into fresh wild-type cells recapitulates the genetic suppression and protection from CSE with relative growth rates and statistical parameters provided in the table. The standard error of the mean (SEM) is provided. (C) Growth rates for *Dictyostelium* transformed with full-length *ancA* (FL-*ancA*) compared to control plasmid with and without 40% CSE. Median bars are shown. Statistics by ANOVA with Fisher's LSD post hoc test. Asterisks indicate $P<0.05$. (D,E) Cell viability and necrosis were assessed in immortalized human bronchial epithelial cells (HBEC3-KTs) with ANT1 and ANT2 overexpression (OE) followed by 24 hrs of 10–80% CSE exposure. Cell count quantification normalized to 0% CSE (D). Apoptosis assessed by annexin-V staining after CSE (E). Data show the mean±s.e.m., $n=16$ from 2–3 experiments. Representative images in Fig. S1. Statistics by ANOVA with Fisher's LSD post hoc test; P -values as indicated in graphs.

result in changes in expression levels of the mitochondrial proteins TOM20, VDACs and COX4 (Fig. S1E). We observed no change in nuclei number per cell (single nuclei per cell), indicating no inhibition of cytokinesis. ANT1 and ANT2 overexpression in HBEC3-KT cells also yielded a small reduction in apoptotic cell death in response to CSE (Fig. 1E; images in Fig. S1G).

ANT expression level is reduced in COPD

We next determined ANT isoform gene expression in human lung tissue from normal versus COPD subjects in genome-wide association studies (GWAS) data from the Lung Genome Research Consortium (LGR; 1RC2HL101715). COPD patients are stratified by COPD severity, determined by the 2007 global initiative of obstructive lung disease (GOLD) classification, i.e. 1, mild; 2, moderate; 3, severe; 4, very severe (Rabe et al., 2007). GOLD stage is based on pulmonary function testing with forced expiratory volume within 1 s (FEV1). *SLC25A4* (ANT1) is significantly reduced in GOLD patients 2–4 and *SLC25A5* (ANT2) is significantly reduced in GOLD patients 3 and 4 (Fig. 2A). *SLC25A6* (ANT3) was not present in this data set. Subject stratification and pulmonary function characteristics are presented in Fig. 2B. This is further supported by gene expression analysis by real time PCR of a separate cohort of patients with and

without COPD, which also revealed a significant reduction in *SLC25A4* (ANT1) and *SLC25A5* (ANT2) in COPD lung tissue (Fig. 2C). *SLC25A5* (ANT2) gene expression was also significantly reduced in ciliated small airway cells isolated from smokers compared to non-smokers in a publicly available GEO dataset (#GDS2486) (Fig. 2D). Although not statistically significant, *SLC25A4* showed a decreasing trend. In a mouse model exposed to cigarette smoke for 6 months (during which mice develop airspace enlargement and airway remodeling), *slc25a5* (*ant2*) gene expression, as assessed by real time PCR, was also reduced in lungs of smoke-exposed C57BL/6 mice compared to air-exposed control mice (Fig. 2E). These collective observations support the notion that ANT2 (*SLC25A5*) expression is reduced by exposure to cigarette smoke, which could contribute to COPD pathogenesis.

ANT regulates cellular respiration and ATP production

Cigarette smoke is thought to cause an oxidative insult to lung epithelium and mitochondria, resulting in metabolic dysfunction and oxidative stress (Hoffmann et al., 2013; Wiegman et al., 2015). ANT proteins are ADP/ATP transporters that reside in the inner mitochondrial membrane where they provide the source of ADP substrate for the ATP synthase to generate ATP (Liu and Chen, 2013). The ANT proteins then return the ATP to the cytoplasm

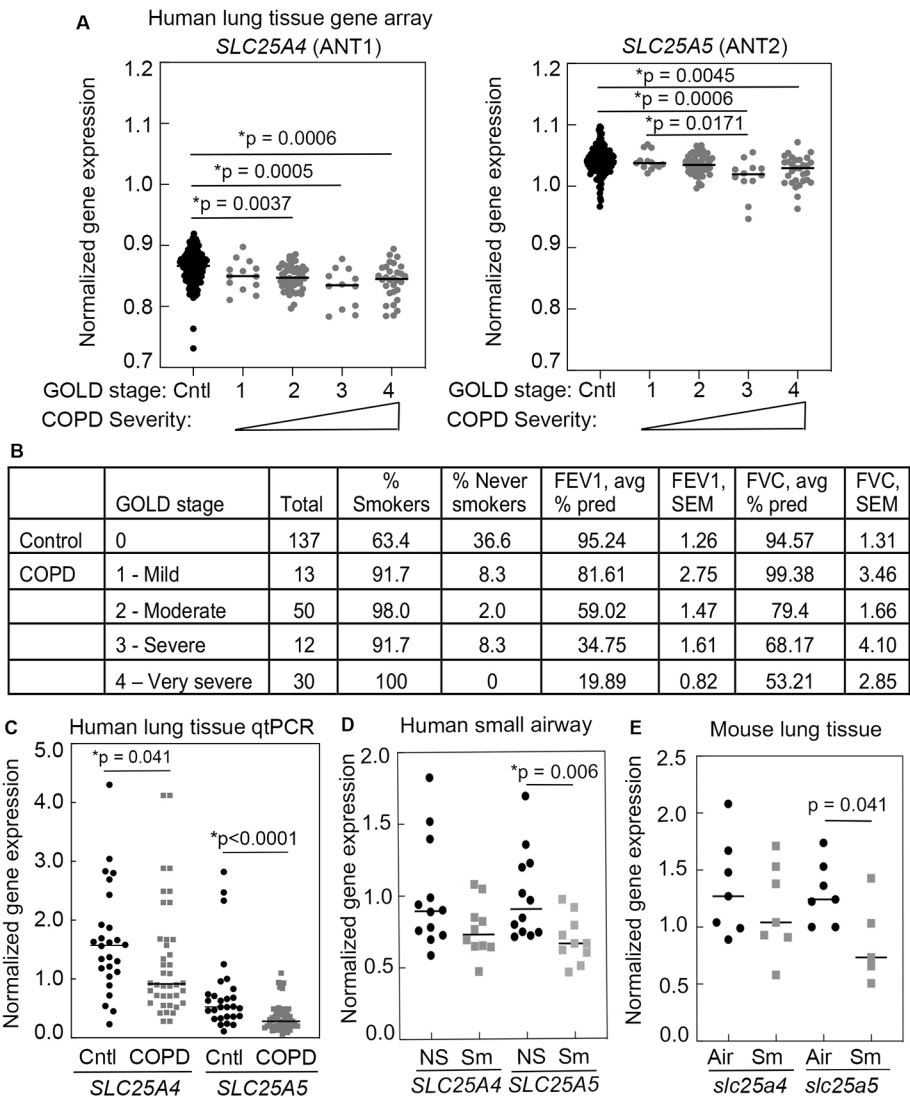


Fig. 2. ANT expression is reduced in COPD patients, smokers and a mouse model of COPD. (A) Human GWAS gene expression data for *SLC25A4* (ANT1) and *SLC25A5* (ANT2) in healthy ($n=137$ subjects) versus COPD patient whole-lung tissue, normalized to glucose-6-phosphate isomerase (GPI). Subjects were stratified by COPD severity as defined by GOLD severity stage (1, mild; 2, moderate; 3, severe; 4, very severe). Median bars are shown. Statistics by Kruskal–Wallis with Mann–Whitney post hoc test; P -values as indicated. (B) Control and COPD patient characteristics including forced expiratory volume in 1 s (FEV1, percentage predicted) and forced vital capacity (FVC, percent predicted). The standard error of the mean (SEM) is provided. (C) Gene expression of *SLC25A4* and *SLC25A5* in whole-lung tissue from healthy humans ($n=28–29$) versus COPD patients ($n=20–23$) assessed by real-time PCR, normalized to β -actin. Statistics by Student's t -test; P -values as indicated. (D) GWAS gene expression data for *SLC25A4* and *SLC25A5* in human small airway epithelial cells from non-smokers ($n=12$ subjects) versus smokers ($n=10$), normalized to GPI, GEO database GDS2486. Medians are shown. Statistics by ANOVA with Mann–Whitney post hoc test; P -values as indicated. (E) *Slc25a4* (*ant1*) and *Slc25a5* (*ant2*) gene expression in air versus smoke-treated mouse lungs (6-month exposure), Normalized ΔCt , $n=7$ per group, normalized to GAPDH. Statistics by Mann–Whitney, with P -values as indicated.

where the ATP is utilized as the energy currency of the cell. ANT2 can also reverse this direction to provide ATP substrates to assist the ATP synthase to restore the proton-gradient across the mitochondrial inner membrane. Given the changes in ANT expression found in COPD lung tissue (Fig. 2) and that cigarette smoke can cause mitochondrial dysfunction (Wiegman et al., 2015), we tested whether ANT modulation impacts the metabolic activity of intact airway epithelial cells, as well as the impact of CSE on the energy state of the cell. During oxidative phosphorylation (OXPHOS) and in the presence of NADH and FADH₂, electrons are passed along the electron transport chain (ETC) that comprises a series of four complexes (I–IV), to reduce O₂ to H₂O. This electron gradient is then utilized by complex V (i.e. ATP synthase) to convert ADP to ATP. The oxygen consumption rate (OCR) can be measured after the addition of ETC complex inhibitors (Fig. S2A) to determine basal mitochondrial respiration (OCR in absence of inhibitors), ATP production (indirect measure of ATP via OCR that is sensitive to inhibition of complex V with oligomycin) and spare respiratory capacity (difference between maximal OCR in the presence of the protonophore FCCP and basal respiration). ATP synthase also uses ATP hydrolysis to pump protons into the inner mitochondrial membrane, providing another means to generate the proton gradient. Protons can also move back into the matrix independent of the ATP synthase, resulting in a ‘proton leak’ that results in partial uncoupling of oxygen consumption from ATP production and is thought to occur in part through ANT proteins (Jastroch et al., 2010). Proton leak can be determined by the difference between the OCR upon addition of oligomycin versus the OCR after addition of the complex I and III inhibitors rotenone and antimycin A. In addition, the extracellular acidification rate (ECAR) provides insight into the relative importance of OXPHOS versus glycolysis for cellular ATP production (acidification due to increased production of lactate when glycolytic demand is high).

We found that increased protein levels of ANT1 or ANT2 in HBEC3-KT cells (Fig. S1E,F) result in increased basal oxygen consumption (26±5.7% or 22±6.1%, respectively) and higher spare respiratory capacity (14±7.2% or 23±6.2%, respectively) in the cells (Fig. 3A; also see Fig. S2B,C). These increases led to a cellular phenotype characterized by enhanced mitochondrial respiration (OCR) and glycolytic flux or ECAR (Fig. 3B). Consistent with the notion that ANT proteins provide one means by which proton leak can occur (Jastroch et al., 2010), ANT1 overexpression resulted in increased proton leak, although we did not observe this effect in ANT2-overexpressing cells (Fig. S2D). Overall, CSE had a statistically significant impact on the metabolic state of the cell, decreasing maximal oxygen consumption by 24±2.8% without a significant change in basal respiration (Fig. S2B,C). The enhanced OCR due to ANT overexpression (baseline and maximal OCR) was maintained after 4 h of CSE exposure but dropped in control cells (Fig. S2C). The increase in aerobic respiration for ANT2-overexpressing cells was, in turn, reflected by increased mitochondrial ATP production (oligomycin-sensitive respiration), 22±5.6% compared with control (Fig. 3C). However, steady-state intracellular ATP concentrations in HBEC3-KT cells overexpressing ANT2 were unchanged at 8 mM (Fig. S2H). Interestingly, this concentration is considered to be at the higher end of the spectrum when compared with measurements in various cell types.

Knockdown of ANT1 and ANT2 gene expression by using small interfering RNA (siRNA) resulted in significant reduction in basal oxygen consumption, maximal OCR and ATP production (Fig. 3D, F; Fig. S2E,F), and increased glycolysis or ECAR (Fig. 3E). We

observed no significant change in proton leak upon ANT1 or ANT2 siRNA knockdown (Fig. S2G). Suppression of ANT gene expression by using siRNA specifically targeting each isoform resulted in reductions in ANT1 and ANT2 protein levels (61% and 74%, respectively) (Fig. S3A). However, ANT2 siRNA appears to also significantly reduce ANT1 protein levels (Fig. S3A). Expression levels of mitochondrial proteins in HBEC3-KT cells, i.e. TOM20 (outer mitochondrial membrane), VDACs (outer mitochondrial membrane) and COX4 (inner mitochondrial membrane), did not change upon overexpression (Fig. S1E) or silencing (Fig. S3B) of ANT1 or ANT2, suggesting that the observed metabolic changes are not due to changes in the levels of these mitochondrial proteins. Other studies have found similar stability in regard to OXPHOS proteins (Lu et al., 2017).

Two ANT-specific inhibitors exist that block the ADP/ATP transport function of ANTs, i.e. the cell membrane-impermeable carboxyatractylide (CATR) and the membrane-permeable bongkrekic acid (BKA). ATP production and basal oxidative respiration were halted after treatment with BKA, but CATR had no effect (Fig. 3G,H) – which was anticipated due to its membrane-impermeability. We noticed that basal respiration was inhibited more by BKA than oligomycin (Fig. 3H versus 3A). This might be owing to the ability of BKA to block ANT-mediated proton leak and/or indicate that ANT proteins exert a higher degree of respiratory control in HBEC3-KTs. Thus, ANT proteins, predominantly ANT2, appear to protect cells from CSE, in part by enhancing both mitochondrial respiration and glycolytic flux of the cells, thereby increasing cell survival.

Studies suggest that ANT influences the cellular oxidative state (Kretova et al., 2014; Pan et al., 2015). ANT1 deficiency leads to increased cardiac oxidative stress and cardiomyopathy (Esposito et al., 1999; Graham et al., 1997), whereas overexpression is protective against cardiac ischemic injury (Klumpe et al., 2016; Lynn et al., 2010; Winter et al., 2016). Overexpression of ANT2 is also protective against oxidative stress in hepatocytes (Kim et al., 2012). Therefore, we examined whether changes in ANT levels alter superoxide levels in mitochondria in the context of CSE exposure. In our studies, HBEC3-KT cells did not experience a significant increase in reactive oxygen species (ROS) upon CSE exposure, but ANT1 and ANT2 expression slightly increased the production of mitochondrial superoxide (MitoSOX) (Fig. S2I). However, it should be noted that this experiment was performed by using a high-content imager, allowing it to be so heavily powered that a change of only few percentage points might appear statistically significant. Nevertheless, we suspect that this slight elevation in ROS after overexpression of ANT1 or ANT2 may reflect increased flux through the electron transport chain, resulting in elevated production of ATP through expression of these proteins.

ANT2 enhances airway surface hydration and ciliary beat frequency

One of the key functions of the airway epithelium is to clear particles out of the lung through mucociliary clearance and ciliary beating, processes that are both dysfunctional in COPD due to cigarette smoke (Elliott et al., 2007; Simet et al., 2010). The normal human airway is lined with ciliated airway epithelial and mucosal cells that comprise an overlying ASL layer (Bustamante-Marin and Ostrowski, 2017). The hydration status of the ASL and a coordinated ciliary beating are important in maintaining adequate clearance and airway homeostasis. Cilia depend on ATP, not only for energy but also as a signaling molecule that influences airway surface hydration (Button et al., 2008, 2013; Lazarowski et al.,

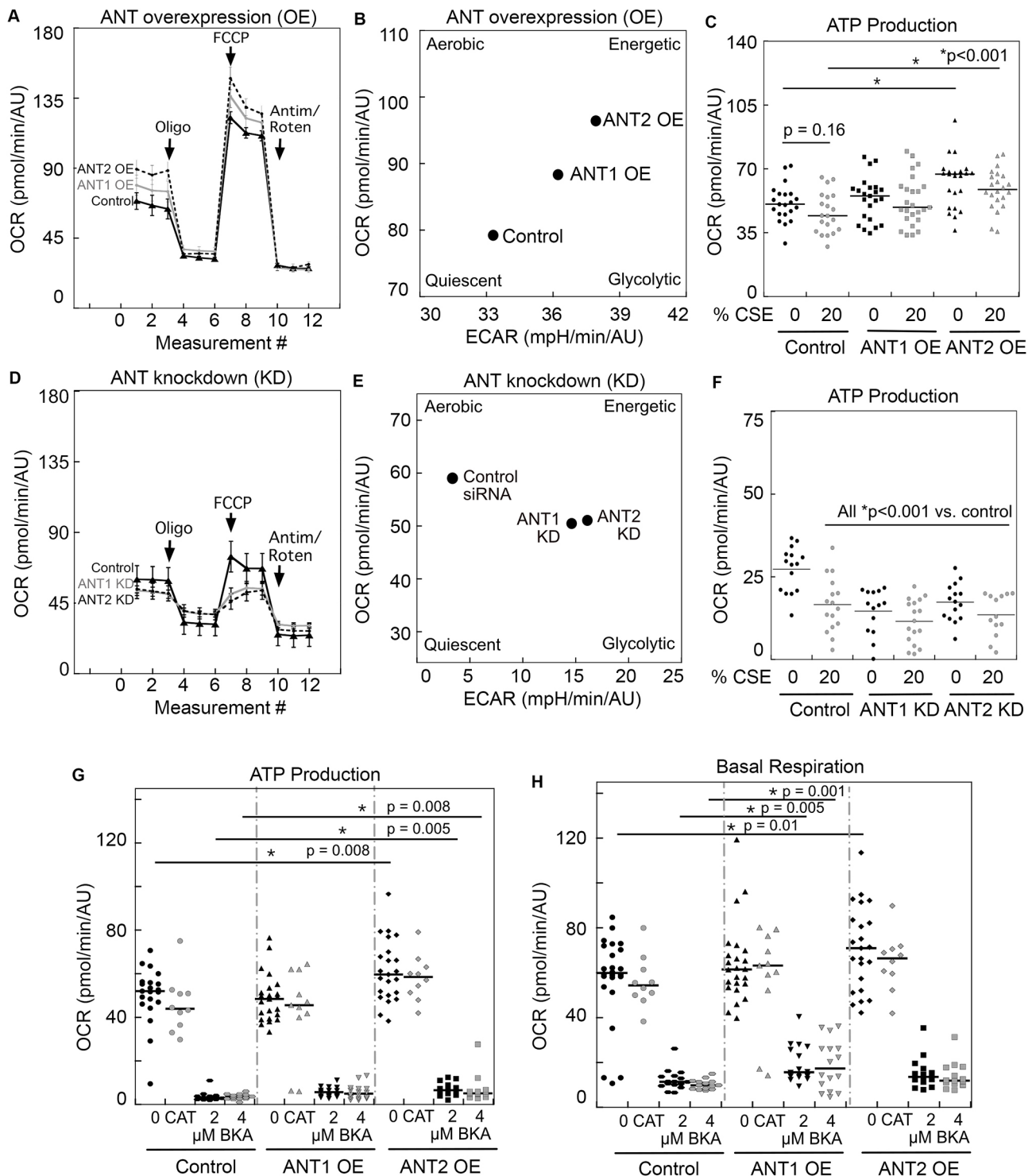


Fig. 3. ANT regulates respiration and ATP production in human bronchial epithelial cells. (A–F) HBEC3-KT cellular metabolism was measured using the Seahorse assay in cells that overexpress (OE) ANT1 or ANT2 (A–C), and in cells in which ANT1 or ANT2 was knocked down (KD) by siRNA (D–F). Oxygen consumption rates (OCRs) were assessed over time (A,D); the mean \pm s.e.m. is provided for each measurement. OCRs versus extracellular acidification rates (ECAR) are shown in B and E. A shift towards a more energetic state was found in ANT OE cells (B), whereas a shift towards a less aerobic state was observed in ANT KO cells (E). Production of ATP was increased upon ANT overexpression (C) but decreased when ANT was knocked down (F); as shown in dot plots, with median values indicated by bars ($n=15$ –26 wells from three experiments). (G,H) ANT was overexpressed by using adenovirus in HBEC3-KT cells with or without 20 μ M CATR, or 2 and 4 μ M BKA. Seahorse assay analysis shows ATP production (G) and basal OCR (H). Statistics by ANOVA with Fisher's LSD post hoc test; * $P<0.05$, unless indicated otherwise.

2004). Extracellular ATP regulates airway surface hydration by the direct activation of P2Y purinergic receptor signaling that inhibits the epithelial Na^+ channel (ENaC) and Na^+ absorption, while

activating Cl^- movement through the cystic fibrosis transmembrane conductance regulator (CFTR) (Ma et al., 2002). The resulting ion flux generates an osmotic gradient that drives H_2O from epithelial

cells to hydrate the overlying ASL (Ma et al., 2002). Hydration of the ASL reduces mucus viscoelasticity, promoting mucus clearance and proper ciliary function, both of which are negatively impacted by cigarette smoke and become dysfunctional in COPD (Clunes et al., 2012; Leopold et al., 2009; Maestrelli et al., 2001; Simet et al., 2010; Yaghi et al., 2012).

We utilized primary ciliated normal human bronchial epithelial (NHBE) cells and HBEC3-KTs cultured at air-liquid interface (Hoffmann et al., 2013) to determine the impact of ANT on ASL thickness and ciliary beat frequency (CBF) in cells that overexpress ANT1 or ANT2. Primary NHBE cells were isolated from human lungs and differentiated to generate cilia with a mucous layer under conditions of air liquid interface (ALI), recapitulating the human airway. ANT2 overexpression by adenovirus in NHBE cells resulted in a 2.3-fold increase in ASL thickness compared to that of control and ANT1-overexpressing cells (Fig. 4A). Stable overexpression of ANT2 by using lentivirus (Fig. 4B) similarly yielded an increase in ASL hydration (Fig. 4C). Importantly, this increase in ASL hydration thickness was inhibited by the cell membrane-impermeable ANT inhibitor CATR (Fig. 4C). Upon adenoviral overexpression of ANT2, CATR or the cell membrane-permeable BKA also inhibited any increase in ASL (Fig. 4D,E), which is in contrast to the differential impact of these compounds on metabolic activity and cellular respiration, where only BKA inhibited ATP production and basal respiration (Fig. 3G,H). In addition, treatment with apyrase to remove extracellular ATP reversed the change in ASL induced by ANT2 overexpression (Fig. 4D,E). These findings suggest that enhanced ASL is mediated through extracellular ATP. Control virus-treated cells administered with CATR also trended towards a decrease in ASL, suggesting that endogenous ANT may help mediate basal airway ASL homeostasis. ANT2 also enhanced ASL height in HBEC3-KT cells – a bronchial epithelial immortalized cell line that does not differentiate to form cilia under these conditions – although without reaching statistical significance ($P=0.06$) (Fig. 4F,G). However, the height of ASL in ANT2-overexpressing cells was significantly abrogated upon treatment with BKA ($P=0.01$) and CATR ($P=0.02$) (Fig. 4F,G). Cultures of differentiated NHBE cells comprise several key cell types, namely ciliated epithelial cells, secretory mucin-producing cells and basal cells (Dvorak et al., 2011). These observations indicate that ANT2 is important for ASL regulation even in non-ciliated epithelial cells and is, therefore, not dependent on the presence of ciliary structures.

Because ANT2 overexpression increases and protects ASL height, we hypothesized that ANT2 might also protect ciliated airway epithelial cells from a reduction in CBF caused by exposure to acute cigarette smoke. In fact, ANT2 also protected CBF, and this protection persisted after a rest period (Fig. 5A,B). ANT overexpression did not alter baseline CBF, and air exposure alone did not significantly alter CBF in all groups (Fig. S4A–C). Videos of ciliary beating before and after exposure to cigarette smoke for control, and ANT1- or ANT2-overexpressing cells are provided (Movies 1–6).

Upon differentiation, ALI cultures become composed of multiple cell types, including ciliated cells, mucin-producing cells and basal cells, and we wondered whether overexpression of ANT1 or ANT2 can shift the distribution of cell types. To test this, we quantified the fraction of ciliated cells that are moving in each field and were used to assess CBF. Transient overexpression of ANT1 or ANT2 in primary NHBE cells did not alter the fraction of ciliated cells present in ALI cultures (Fig. 5C). To evaluate the fraction of mucin-producing cells, we checked the expression of

mucins, specifically of the two most secreted airway isoforms MUC5AC and MUC5B. Lentiviral overexpression of ANT2 did not change mRNA expression of *MUC5AC* and *MUC5B* (Fig. 5D). Collectively, acute expression of ANT1 or ANT2 does not appear to significantly shift the distribution of cell-types in the ALI cultures.

ANT localizes to the plasma membrane in ciliated airway epithelium

Because membrane-impermeable CATR inhibited enhancement of ASL by ANT2 but not its effect on mitochondrial respiration, we hypothesized that ANT proteins are likely to be distributed in the plasma membrane, where they mediate this ATP-dependent impact on ASL. Literature indicates that, in the extracellular ASL of airway epithelial cells, ATP levels are ~4–10 nM (Button et al., 2008, 2013; Lazarowski et al., 2011; Seminario-Vidal et al., 2011). When compared to the ~8 mM total intracellular ATP measured for HBEC3-KT cells (Fig. S2H), this results in a $\sim 10^5$ – 10^6 -fold concentration gradient across the plasma membrane, i.e. much steeper than the gradient of most other ions involved in the chemiosmotic cycle. With such a steep gradient, different regulatory mechanisms are likely to modulate ATP movement through transporters – such as ANT proteins at the plasma membrane – versus how ANT is regulated at the mitochondrial membrane.

Therefore, we next examined the cellular distribution of ANT proteins in the airways of human and mouse lung tissue to determine how ANT expression varies at baseline and in the context of COPD. In human airway epithelial cells, mitochondria are enriched at the apical side of the cell layer. As expected, ANT1 (Fig. 6A left panels, arrowhead) and ANT2/3 (Fig. 6A right panels, arrowheads) are present near the apical side of the airway pseudo-stratified columnar cells, where mitochondria are enriched (Fig. 6A, arrowheads). Here, ANT1 and ANT2/3 colocalize with the mitochondrial proteins COX4 (colocalization with ANT1 in Fig. 6B, arrowhead; ANT2/3 in Fig. S5A) and TOM20 (Fig. S5B). Unexpectedly, we also observed ANT1 (Fig. 6A left panels, arrows) and ANT2/3 (Fig. 6A right panels, arrows) located outside the boundaries of mitochondria at the region of the apical plasma membrane that extends along the ciliary plasma membrane. Previously, ANT and another canonical inner mitochondrial membrane protein ATP synthase F1 subunit β , have been observed at the plasma membrane in hepatocytes (Cardouat et al., 2017) and endothelial cells (Martinez et al., 2015; Radojkovic et al., 2009), respectively. However, so far, ANT protein localization in lung epithelium has been unknown. In human airway epithelial cells, we observed that ANT proteins are also present at the plasma membrane (Fig. 6C, arrowhead) with a portion that colocalizes with acetylated α -tubulin at the cilia of the cells (Fig. 6C, arrow). We found no evidence of fluorescence bleed-through for either α -tubulin or TOM20 (Fig. S5C). Similarly, ANT2/3 protein colocalized with acetylated α -tubulin in human airway tissue (Fig. S5A).

To confirm, we detected the distribution of this plasma membrane protein, we used six different antibodies raised against ANT1 and ANT2 in human airway tissue from normal human lung. The full antibody panel may be found in Fig. S6 (with a representative analysis in Fig. S6B and ciliary layer versus mitochondrial quantification in Fig. S6C,D). We found different specificity for the various ANT isoforms by western blotting for each of the human isoforms, i.e. ANT1–4, expressed in yeast (Fig. S3C). Overall, these data indicate that a subset of ANT proteins are distributed in the apical plasma membrane region in addition to the canonical mitochondrial distribution.

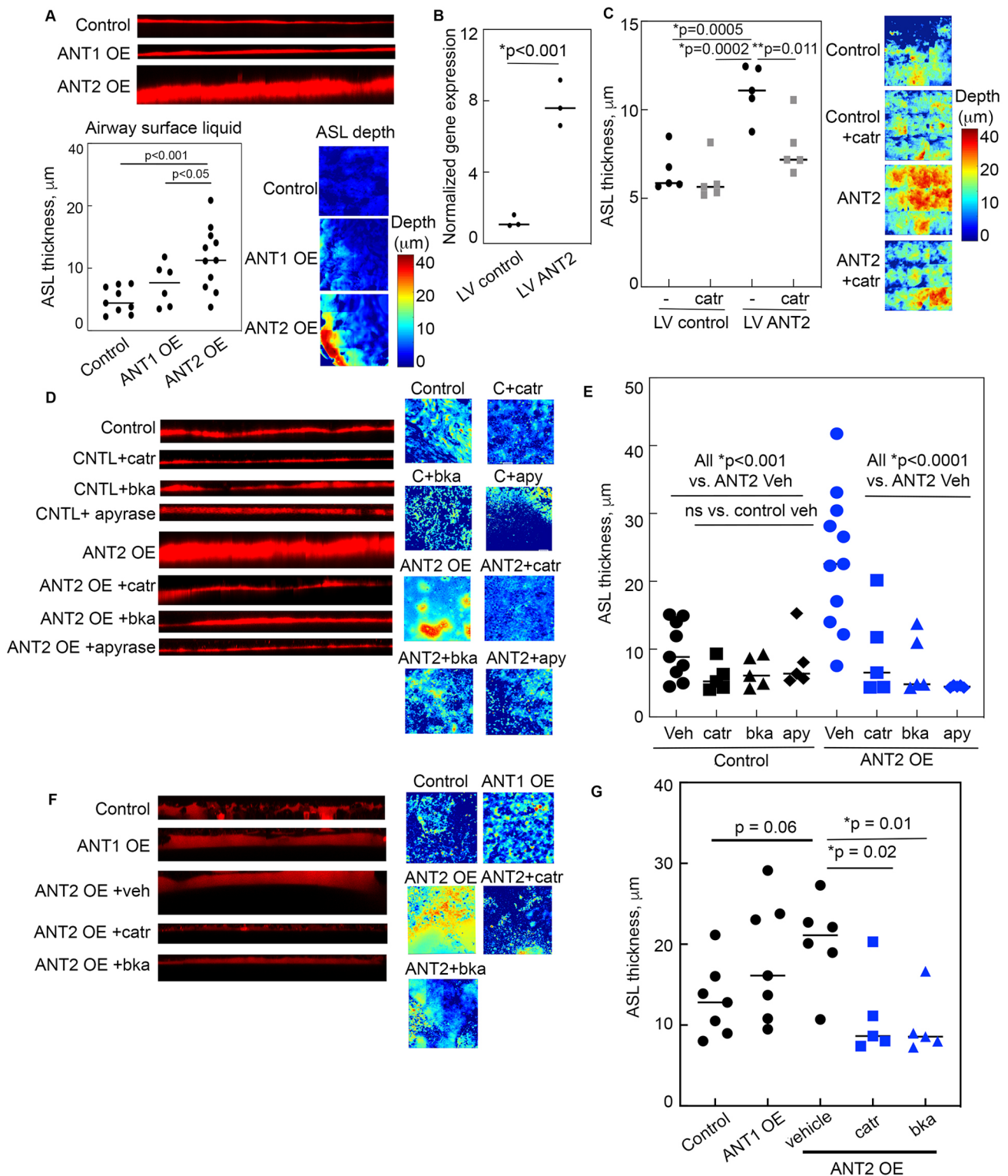


Fig. 4. ANT2 enhances ASL hydration and preserves CBF after cigarette smoke. (A) ASL height in NHBE cells from a healthy human donor with control adenovirus or adenoviral overexpression (OE) of human ANT1 or ANT2. Representative z-stack of orthogonal views of ASL height with depth heat maps. $n=6-11$ ALI cell inserts from three humans. P -values as indicated. (B) *SLC25A5* (ANT2) gene expression after lentiviral (LV) overexpression of ANT2 in primary NHBE cells. $n=3$ inserts. Statistics by Student's t -test; P -values as indicated. (C) ASL height after lentiviral overexpression of ANT2 with or without treatment with 20 μM CATR. Representative depth heat maps are shown. $n=5$ ALI inserts. P -values as indicated. (D,E) ASL height was determined in primary NHBE cells with adenoviral overexpression of ANT2 (ANT2 OE) versus control virus with PBS vehicle, 20 μM CATR, 4 μM BKA or apyrase (apy). Representative ASL orthogonal views and heat maps (D), and ASL quantification (E). $n=5-11$ inserts from three healthy humans over 2–4 days. P -values as indicated. (F,G) ASL height was determined in HBEC3-KT cells, which do not have cilia, after adenoviral overexpression of ANT1, ANT2 versus control virus with PBS vehicle, 20 μM CATR or 4 μM BKA. Representative ASL orthogonal views and heat maps (F) in HBEC3-KT cells, and ASL quantification (G). $n=5-7$ inserts from two separate experimental days. For statistical analysis of A, C, D, E and G, one-way ANOVA was used followed by a Fisher's LSD post hoc test.

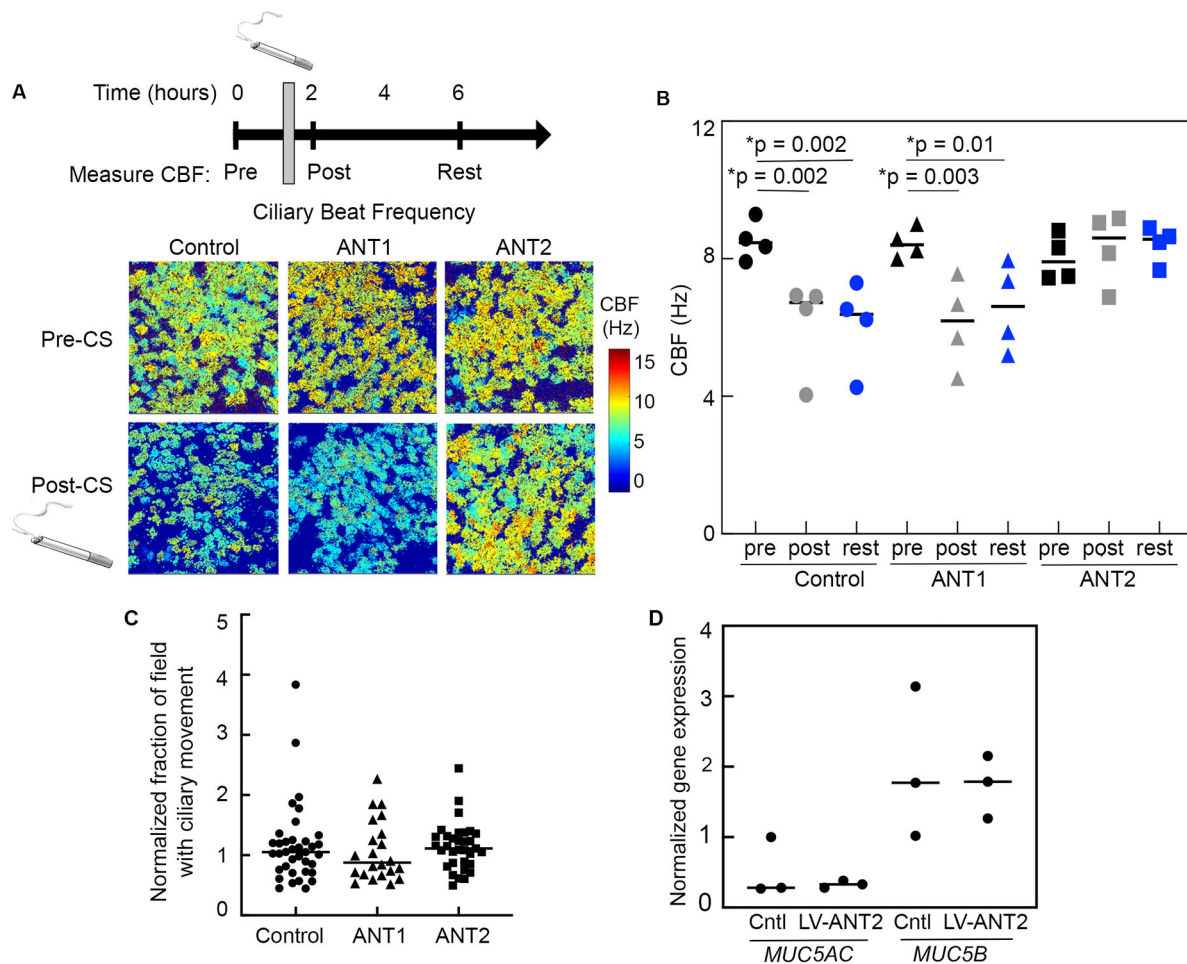


Fig. 5. ANT2 preserves CBF after cigarette smoke. Quantification of CBF measured in control NHBE cells and ANT1- or ANT2-overexpressing NHBE cells before or after exposure to cigarette smoke (CS), 30 min post-treatment, or 4 h rest. (A) Experimental setup and example CBF heat maps from the 30-min post-CS time point. CBFs from control air-exposed NHBE cells are provided in Fig. S4. (B) Quantification of CBF. Medians are provided. P -values determined by ANOVA with Fisher's LSD post hoc test; P -values noted. (C) For each pre-exposure CBF image, the percentage of the total image area that contains ciliary movement was determined (CBF images are exemplified in A). All images were normalized to control NHBE cells. No statistical differences were present as determined by one-way ANOVA with Fisher's LSD post hoc test. All CBF data are representative of three distinct human donors for ALI cultures that were assayed on three different days with $n=2-3$ inserts per time point. (D) Human *MUC5AC* and *MUC5B* gene expression after lentiviral overexpression of ANT2 in primary NHBE cells, $n=3$ inserts. No statistical differences were present as determined by a Student's t -test.

In human COPD airway tissue, the ANT2/3 signal seems to be reduced in mitochondrial and ciliary plasma membrane regions compared to normal control tissue, which, however, does not meet statistical significance (Fig. 6D, quantification in Fig. S5D). Similarly, we observed ANT proteins at the plasma membrane in primary ciliated NHBE cells grown on ALI, derived from four human patients (Fig. 6E, panel of antibodies tested in Fig. S7). To confirm the plasma membrane localization of ANT proteins, ALI cultures were first probed with an antibody against ANT2/3 followed by secondary antibody conjugated to Alexa Fluor 555, with or without permeabilization, then stained again with the same primary antibody (secondary antibody conjugated to Alexa Fluor 488). ANT2 was concentrated at the plasma membrane, outlining the cell borders at the apical surface in ALI cultures within both permeabilized and non-permeabilized samples (Fig. 6F permeabilized; ab222843, Fig. S8A non-permeabilized, S8B), with similar findings for ANT1 (ab102032, Fig. S8C).

We then expressed ANT2 conjugated to GFP (ANT2-GFP) by using lentivirus in NHBE cells that were then differentiated in ALI culture. The GFP signal from ANT2-GFP was detected at the ciliary

membrane and colocalized with acetylated α -tubulin staining (Fig. 7A). When control lentivirus-mediated expression of GFP alone was used, the GFP signal at cilia was absent. For comparison and to help confirm that the GFP fusion did not disrupt ANT2 targeting, we expressed ANT2-GFP in HBEC3-KT cells that do not form cilia. In this context, ANT2-GFP specifically colocalized to mitochondria (detected using mitotracker dye). However, GFP alone (GFP-expressing control cells) did not label mitochondria (Fig. S8D, arrowheads).

Mice show a similar cell-type expression of the ANT paralogs 1, 2 and 4 to that in humans. We looked at ANT1 and ANT2 localization in the mouse airway epithelium and found murine ANT present at the plasma and ciliary membranes of airway cells (Fig. 7B, arrows). Structured illumination microscopy of ANT 1 in mouse airway epithelium indicated a highly patterned distribution along apical cell surface, the base of cilia and the periciliary membrane (Fig. 7C, arrows; Movie 7). In mice exposed to cigarette smoke for 6 months, this ANT pattern was disrupted with less organized ANT distribution at the plasma membrane compared to air-treated control mice (Fig. 7C; Movie 8). Further, airway

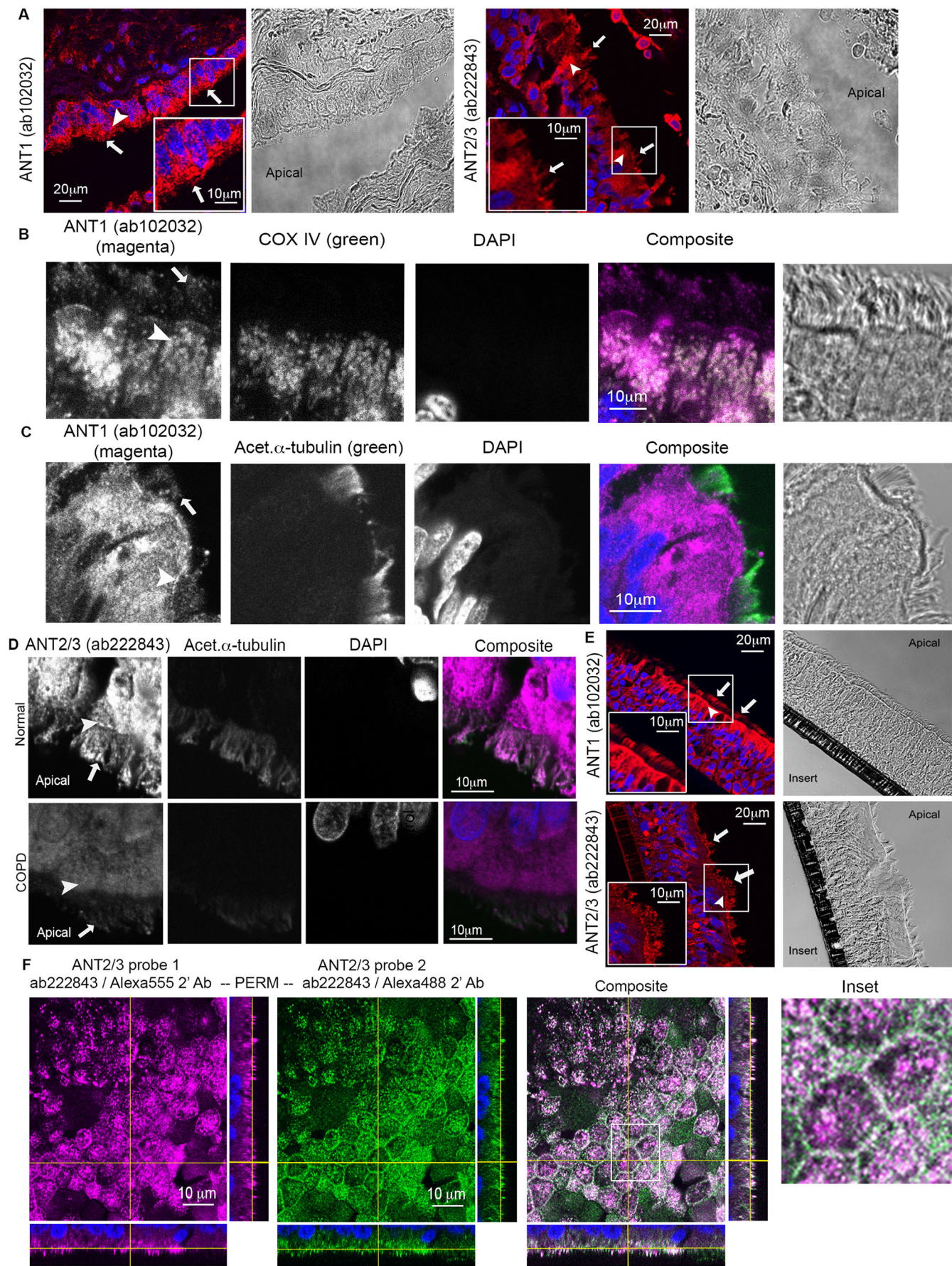


Fig. 6. See next page for legend.

Fig. 6. ANT localizes to the plasma membrane in ciliated airway epithelium. (A) Normal human airway tissue stained for ANT1 (first image) or ANT2/3 (third image) and imaged by confocal microscopy. ANT (shown in red) localized to mitochondria (arrowheads) and the ciliary layer (arrows). Representative of $n=3-4$ different subjects. A magnified view of the boxed area is shown in the left or right corner of the respective image. (B) ANT1 (magenta; stained in 555 channel) colocalization with COX4 (COX IV, green, stained in 647 channel) is indicated by an arrowhead. ANT1 at the ciliary layer is indicated by an arrow. (C) ANT1 (magenta, stained in 555 channel) colocalization with acetylated tubulin (green, stained in 647 channel) at the plasma membrane (arrowhead) and ciliary layer (arrow). (D) Human lung tissue from control and COPD patients stained for ANT2/3 (magenta, 555 channel) and acetylated tubulin (647 channel). ANT2/3 localized to mitochondria is indicated by an arrowhead, and ANT2/3 localized to the ciliary layer is indicated by an arrow. Representative of $n=3-5$ subject per group. (E) NHBE cells grown at ALI and stained for native ANT1 or ANT2/3, demonstrating localization of ANT to the mitochondrial layer (arrowhead) and ciliary layer (arrow). A magnified view of the boxed area is shown in the right corner of the image. (F) ANT2/3 localizes to the plasma membrane in NHBE cells. NHBE cells were stained for ANT2/3 (without prior permeabilization) followed by secondary antibody conjugated to Alexa Fluor 555 (magenta), then permeabilized and stained again with anti-ANT2/3 followed by secondary antibody conjugated to Alexa Fluor 488 (green). The boxed area in the composite image is shown enlarged on the right. $n=3$ inserts. Representative images of non-permeabilized cells are shown in Fig. S8A. Nuclei were stained with DAPI. All images were taken with a confocal microscope.

epithelial cells from *Ant1*-null mice (Graham et al., 1997) had significantly less plasma membrane staining compared to wild-type mice using ANT1 antibody ab102032 (Fig. 7D). However, the remaining staining showed a similar pattern, which may be due to the fact that this antibody also partially recognizes the ANT2 paralog (Fig. S7). The plasma membrane localization of ANT1 was not a generalized pattern in all ciliated cells. Non-motile cilia of the olfactory epithelium in mice did not have ANT located at the plasma membrane, whereas neighboring motile respiratory epithelia contain ANT at the apical plasma membrane in the same mouse tissue sections (Fig. 7E).

In summary, this discovery of ANT protein at the plasma and ciliary membranes, and the effect of ANT2 on ASL and CBF suggests that ANT also helps to mediate ATP transport at the plasma membrane. Pannexin-1 has already been implicated in providing part of the ATP transport in healthy airways (Lazarowski and Harden, 1999; Okada et al., 2006; Seminario-Vidal et al., 2011). The presence of ANT at the plasma membrane, which CATR inhibits, is likely to provide another mechanism of ATP transport at the airway surface, which – in turn – promotes an increase in ASL height and protects ciliary beating when challenged by cigarette smoke.

DISCUSSION

By utilizing a powerful model organism platform extending from *Dictyostelium* to the human lung disease COPD, we have discovered that the canonical inner mitochondrial membrane protein adenine nucleotide translocase contributes to key functions in airway epithelial biology (Salvioli et al., 2013). Namely, ANT plays multiple roles, including the protection of cell viability by enhancing mitochondrial respiration, promotion of airway hydration and preservation of ciliary function (Fig. 8). Regarding COPD, prior studies suggest an important role for mitochondrial dysfunction in the response to cigarette smoke (Hoffmann et al., 2013; Wiegman et al., 2015). Here, we found that, by manipulating ANT expression, mitochondrial respiration and glycolytic flux can be increased, which allows cells to withstand injury and prevent subsequent cell death in response to insults, such as cigarette smoke. The metabolic role of ANT proteins may be primarily responsible

for this protection because ANT proteins can protect the growth of *Dictyostelium* cells, which do not have cilia and no apparent plasma membrane-associated ANT. Expression levels of ANT appear to help overall cellular respiration and ATP production in airway epithelial cells. In further support of the key role of ANT2 in airway biology and COPD, we found that *SLC25A5* (ANT2) gene expression is reduced in the lungs of COPD patients from separate human tissue cohorts, specifically in human ciliated airway epithelial cells from smokers, and when using a mouse model of smoke exposure. This highlights the importance to understand how ANT proteins impact COPD pathogenesis.

Usually, ANT proteins are translated in the cytoplasm and imported to the inner mitochondrial membrane, where they transport ADP and ATP. However, we found that ANT1 and ANT2 proteins are also present in the plasma and ciliary membranes of the airway epithelium. It is notable that one prior study, using a proteomics approach, also identified ANT1 as a potential interactor with the ciliary protein UBXD8 (FAF2) (Raman et al., 2015). Our observations are based upon three main lines of evidence. (1) Inhibition to modulate ASL thickness with the cell-impermeable ANT inhibitor CATR; (2) immunocytochemistry and immunohistochemistry by using a library of anti-ANT1 and anti-ANT2 antibodies and; (3) expression of ANT-GFP fusion proteins in primary airway epithelial cells. Our observations support the conclusion that ANT1 and ANT2 proteins reside at the plasma membrane in epithelial cells, where they help to modulate ASL and ciliary function. Interestingly, both ANT1 and ANT2 contain predicted secretion-signal sequences that could be the basis for their plasma membrane insertion.

Our discovery of a subset of ANT proteins that reside and function at the plasma membrane of airway cells indicates that ANT proteins have important non-mitochondrial roles in primary airway epithelium. ANT2, in particular, has a protective role in airway hydration and ciliary beating – two key components of mucociliary clearance that are abnormal when COPD develops in the lung. Mucociliary clearance is crucial for removal of toxins, inhaled particulates and bacteria from the airway, and the maintenance of mucus homeostasis is the first line of defense in the lower respiratory tract. The efficiency of mucociliary clearance depends on the hydration status of the ASL, the ciliary beat frequency and the appropriate production of mucus. Insults, such as chronic exposure to cigarette smoke, lead to decreased levels of ASL, reduced CBF and abnormal cilia (Clunes et al., 2012; Leopold et al., 2009; Simet et al., 2010; Yaghi et al., 2012) (Fig. 8A). These functions are disrupted in airway diseases, such as COPD and cystic fibrosis. We propose that ANT2 is present at the plasma membrane, where it helps to regulate airway hydration by transporting ATP to the extracellular surface and influencing ciliary beating.

Several physiological pathways, including that via pannexin-1 (Seminario-Vidal et al., 2011), exist to regulate ATP levels at the apical surface of the airway epithelium. ANT proteins may also help to maintain the normal ASL height. Although we did not see an overwhelming effect of ANT inhibitors on ASL height at baseline, ANT could be part of a stress response to insults, such as cigarette smoke. In the context of the plasma membrane, ANT transport is likely to be under alternate control because ATP export is probably driven by the steep concentration gradient across the plasma membrane. The consumption of extracellular ATP may then provide the substrate (ADP) that ANT needs to transition back into a conformation that makes it available to transport more cytoplasmic ATP – although this awaits formal testing. Alternatively, hydrogen ions and the pH of ASL might also impact airway surface hydration. At mitochondria, ANT has a role in proton leak across the

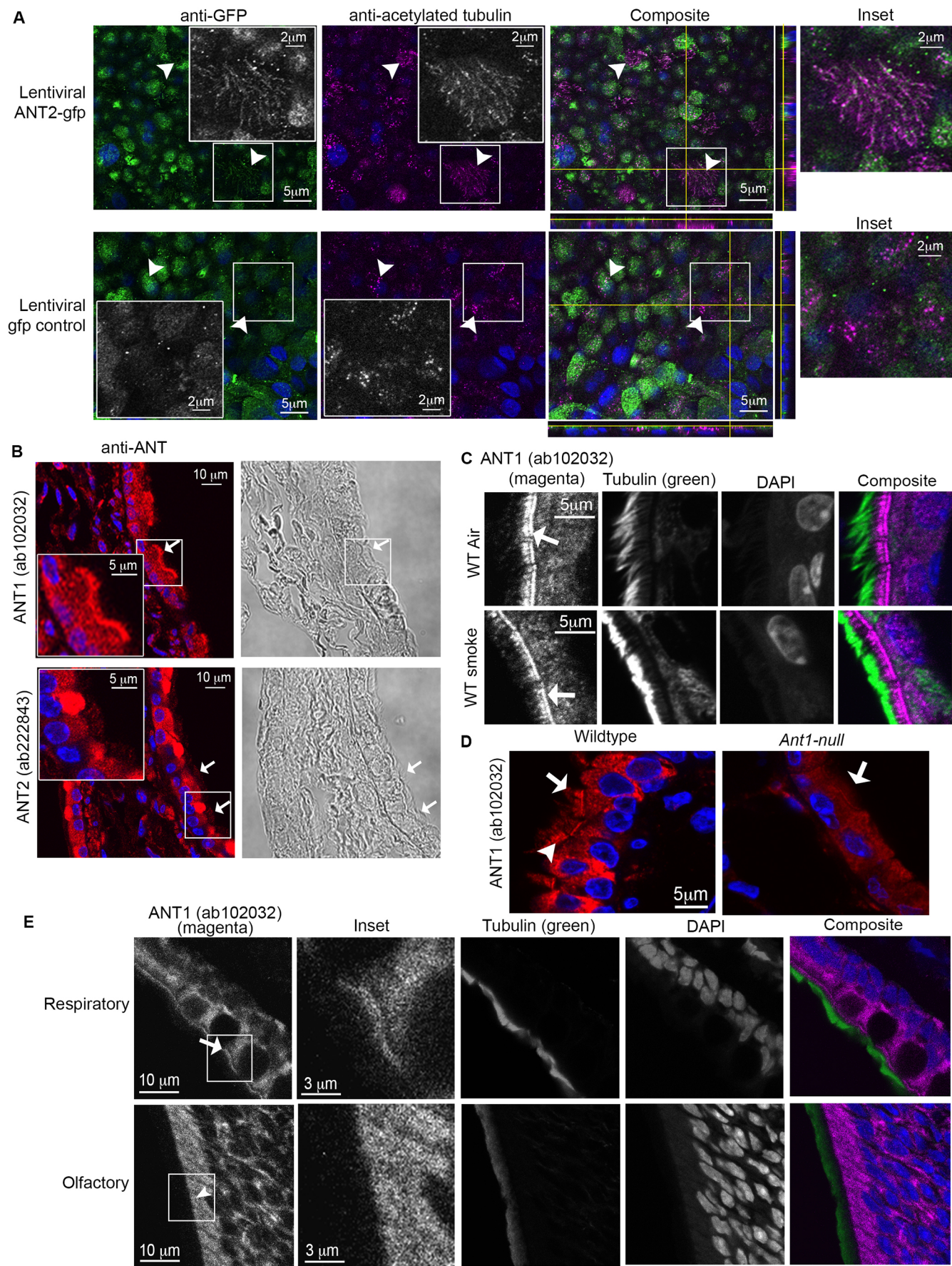


Fig. 7. See next page for legend.

Fig. 7. ANT localizes to the plasma membrane in primary human bronchial epithelial cells and mouse airway epithelium. (A) Lentiviral overexpression of ANT2-GFP and GFP control in differentiated NHBE cells. Cells were stained with anti-GFP (green, secondary antibody conjugated to Alexa Fluor 488) and anti-acetylated tubulin (magenta, secondary antibody conjugated to Alexa Fluor 647) and imaged at the surface by using confocal microscopy. Arrowheads indicate ciliated cells. Grayscale insets are included for each color channel. The boxed area in the composite image is shown enlarged on the right. Representative of $n=3$ inserts per group. (B) Normal mouse airway tissue stained for ANT1 (ab102032) or ANT2/3 (ab222843) and imaged by confocal microscopy. ANT1 (red) localizes to mitochondria and to the plasma membrane/ciliary layer (arrows). Magnified views of the boxed areas are shown bottom or top left of the respective image. Representative of $n=3$. (C) Mouse lungs exposed to air or smoke for 6 months (WT Air or WT smoke, respectively) stained for ANT1 (magenta, ab102032) and acetylated α -tubulin (green), nuclei were stained with DAPI (blue). $n=5$ mice per group. (D) Staining of wild-type C57BL/6EJ and *Ant1* null mouse airways for ANT1 (red, ab102032). Localization of ANT1 at the plasma membrane (arrowhead) and ciliary layers (arrows) is indicated. (E) Mouse upper respiratory and olfactory epithelium stained for ANT1 (magenta) and acetylated α -tubulin (green). Localization of ANT1 at the apical plasma membrane and at mitochondria. The arrow shows a band of ANT1 present at the apical plasma membrane in respiratory epithelium that has motile cilia in comparison to the lower panel with the arrowhead showing ANT only at the level of the mitochondria in olfactory epithelium that has non-motile cilia. Apical membrane ANT is present in motile ciliated respiratory epithelium compared to non-motile ciliated olfactory epithelium. Magnified views of the boxed area in the first images are shown to the right of each image. $n=3$ mice imaged.

mitochondrial membrane and, similarly, could have this function at the plasma membrane, therefore, influencing airway surface hydration (Jastroch et al., 2010). Future investigations could also delineate how ANT inhibitors – specifically CATR – affect other known regulators of ASL hydration and ATP flux, such as pannexin-1, purinergic receptors and CFTR.

In summary, ANT2 is a powerful mediator to alter mitochondrial function by increasing ATP production and manipulating ciliary

function through both airway surface hydration and by preserving ciliary beating (Fig. 8B). This dynamic interplay between hydration of epithelial surfaces and coordinated ciliary beating is important for efficient clearance of mucus and particulates out of the lungs. The discovery of two distinct occurrences of ANT protein in the lung, one in mitochondria and one located at the plasma membrane, imply distinct pathways and will benefit from additional future investigation. Therapeutic modulation of ANT protein levels in the airway epithelium, such as through viral-mediated gene expression or a compound agonist approach, may augment airway surface hydration to alter disease development in COPD patients. Because we found that ANT2 at the plasma membrane regulates the height of ASL in both ciliated and non-ciliated cells, we predict that therapeutics would continue to have a role in smoke-exposed and diseased airways that may have fewer cilia. Moreover, the role of ANT1, mostly ANT2, in cellular metabolism, epithelial surface hydration and ciliary function is likely to have broad applicability and impact in a variety of other lung diseases.

MATERIALS AND METHODS

Further information and requests for resources and reagents should be directed to and will be fulfilled by the corresponding authors.

Genetic selection studies in *Dictyostelium*

Dictyostelium discoideum cells used in our studies were wild-type cells, the HS1000 [Ax3(Rep ORF+7-3)] strain, grown in Hans' enriched HL5 medium [1.4× HL5, containing 8% FM (ForMedium, Norfolk, UK) plus 60 U/ml penicillin, 60 µg/ml streptomycin sulfate] and selected for plasmid transformations with 15 µg/ml G418. Cells were propagated at 22°C on 10-cm Petri dishes. For suspension growth, cells were cultured in 10-ml culture volumes in 125-ml Erlenmeyer flasks under rotation at 180 rpm, 22°C. Cell densities were determined by counting cells on a hemocytometer. The expression cDNA library was constructed in the pLD1A15SN plasmid with a G418 resistance cassette and by using cDNA generated from mRNA isolated from vegetative (growth phase) *Dictyostelium* cells (Robinson and Spudich,

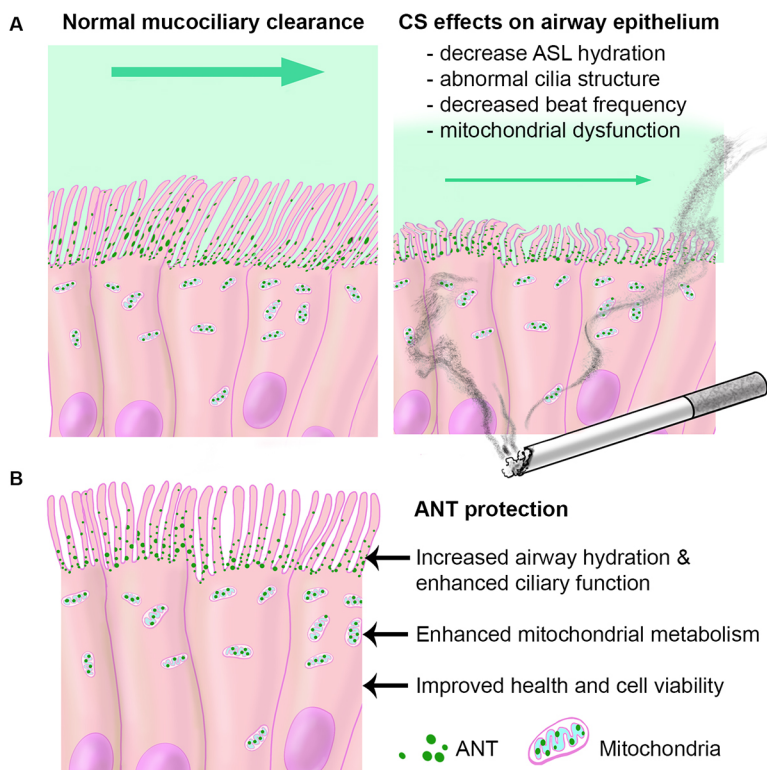


Fig. 8. ANT localizes to motile cilia where ANT2 regulates airway surface hydration and preserve ciliary function.

(A) Normal mucociliary transport requires a delicate balance of airway surface hydration and ciliary beating, to move mucus and particulates out of the lungs. Cigarette smoke (CS) leads to decreased ASL (Clunes et al., 2012), decreased CBF (current data and Yaghi et al., 2012) and abnormal cilia structure (Leopold et al., 2009; Simet et al., 2010), thereby contributing to reduced mucociliary clearance and the development of lung disease.

(B) ANT1 and ANT2 localize to the plasma membrane in ciliated airway epithelial cells. ANT2, specifically, protects human airway epithelium from CS-induced injury by increasing airway surface hydration through ATP regulation, thereby preserving ciliary beat frequency, enhancing metabolism and maintaining cell viability.

2000; Zhou et al., 2010). For a negative control, a GFP-pLD1A15SN plasmid was used. Transformation of wild-type cells was performed using electroporation using a Gene Pulser (BioRad) and a total of 35,000 clones (35 pools of ~1000 clones/pool) were generated. Cells were pulsed once in a 0.4-cm cuvette at 3 μ F. After electroporation, the cells were placed in cold Hans' enriched HL5 to allow recovery and grown for 24 h at 22°C followed by replacement of medium with Hans' enriched HL5 with G418 for growth selection. Medium was changed every 2–3 days until clones were harvested. Cells were initially cultured at 1×10^5 cells per ml in HL5 medium supplemented with G418 alone or with 40% cigarette smoke extract over 3–4 growth cycles. Relative growth rates were determined by counting cells using a hemocytometer. Cell densities were plotted versus time to generate a log phase curve that was exponentially fit using KaleidaGraph (Synergy Software).

The concentration of CSE that results in a 40% decrease in growth rate is reported as the EC40 concentration. DNA was isolated from cultures demonstrating a growth advantage in the context of cigarette smoke, using a glass milk protocol. DNA was transformed into STBL2 cells, and individual clones were selected for DNA clean-up and restriction endonuclease digestion. Recovered DNA was sequenced using standard procedures. cDNA from recovered clones (those showing suppression of the CSE growth phenotype) were transformed into the parent wild-type cells to confirm that the DNA construct could recapitulate the suppression phenotype. Molecular cloning was completed to yield a full length *AncA* plasmid to confirm that suppression of the growth phenotype in the context of 40% CSE in suspension cultures. Primers for full length *AncA* used were included at 1 μ M: forward 5'-AAAAAAGTCGACATGTCTAACCAAA-AGAAAAACGACGTATCTTCATTG-3'; reverse 5'-AAAAAAGCGG-CCGCTTATTTCAGAACCAACACCACC-3'.

Human cell culture – cell lines and primary cells

The human bronchial epithelial cell line (HBEC3-KT, immortalized by Cdk4 and hTERT (Ramirez et al., 2004; a gift from John Minna, University of Texas Southwestern Medical Center, Dallas, Texas, USA) was used for cell viability, metabolic analysis and ASL studies. Cells were verified to be mycoplasma-negative and genetically authenticated by short tandem repeat (STR) profiling (Gene Print 10, Promega). HBEC3-KT cells were maintained in keratinocyte serum-free medium supplemented according to the protocol provided by Lonza (Basel, Switzerland). When 80–90% confluent, cells were split after trypsinization with 0.05% trypsin and neutralization with trypsin neutralizing solution.

Sources of primary normal human bronchial epithelial cells (NHBEs) were the University of Pittsburgh Airway Cell Core, Lonza and MatTek. NHBE cells from a total of five healthy humans were used. Cells attained from the University of Pittsburgh cell core were attained as previously described (Lennox et al., 2018; Myerburg et al., 2010) with a protocol approved by the University of Pittsburgh Investigational Review Board. NHBE cells were grown to 80–90% confluence in collagen-coated flasks then seeded onto type I collagen-coated (50 μ g/ml in 0.02N acetic acid) transparent PET Transwell inserts (0.4- μ m pore, 24-well insert size 0.33 cm² and 12-well insert size 1.12 cm², Corning Costar) at a density of ~5–6 $\times 10^5$ cells/cm². Once a confluent monolayer had formed on the inserts, the apical medium was removed and cells grown at air-liquid interface (Hoffmann et al. 2013) over three to six weeks for differentiation into ciliated airway epithelium.

NHBE cells from Lonza and MatTek were initially grown in growth media, including bronchial epithelial basal medium (BEGM; Lonza) with recommended supplements (bovine pituitary extract, insulin, hydrocortisone, epinephrine, transferrin, recombinant human epidermal growth factor, retinoic acid, triiodothyronine (T3), and gentamicin sulfate amphotericin-B) with additional bovine pituitary extract (12.6 μ g/ml, AthenaES), bovine serum albumin (BSA) (final concentration of 1.5 μ g/ml, Sigma-Aldrich), retinoic acid (final concentration of 0.1 μ M) and epidermal growth factor (final concentration of 25 ng/ml). When NHBE cells were grown at air liquid interface (ALI), basal ALI medium was used including BEGM and Dulbecco's modified Eagle medium (DMEM) with recommended Lonza supplements (one supplement pack per 500 ml of medium) with additional bovine pituitary extract (12.6 μ g/ml, Lonza and AthenaES), BSA (final

concentration of 1.5 μ g/ml, Sigma-Aldrich), and retinoic acid (final concentration of 0.1 μ M).

In vitro cigarette smoke exposure

Methods used for cigarette smoke exposure included prepared cigarette smoke extract (CSE) or gaseous smoke using a Vitrocell exposure chamber. CSE was made by using a peristaltic pump that smoked one research grade cigarette (Tobacco Health Research Institute, University of Kentucky, Lexington, KY) over 6 min, blown into 25 ml of cell-specific media, yielding what was considered 100% CSE, which was then filtered with a 0.22- μ m filter. Doses of CSE from 10–80% were made and used within 6 h. The Vitrocell smoke exposure chamber was used to expose NHBE cells at ALI to humidified air or cigarette smoke. A single exposure is considered air for 16 min or two cigarettes over 16 min using an International Organization for Standardization (McElvaney et al., 1989) protocol.

Targeted gene delivery or suppression

Adenovirus constructs were developed for gene delivery of control eGFP, ANT1-GFP (Ad-h-*SLC25A4*/eGFP, GenBank BC008664.1), and ANT2-GFP (Ad-h-*SLC25A5*/eGFP, GenBank BC056160.1) from Vector Biolabs (Malvern, PA) in NHBE and HBEC3-KT cells. In select ASL studies, lentiviral constructs (Vector Builder Inc.) were used in NHBE cells including control GFP (LVM (VB160109-10005) and ANT2-gfp [#LVS(VB190613-1074dha)-C] at an MOI of 20. NHBE cells were infected with lentivirus for 24 h at the time of seeding onto Transwell inserts, followed by puromycin antibiotic resistance selection for 48 h. The cells were then differentiated at ALI as described. For each cell type, a multiplicity of infection (MOI) titration was completed. Protein expression and localization were confirmed. Adenoviral and lentiviral infection efficiencies were ~85–95% with confirmed expression of ANT-GFP isoforms. Adenoviral infected cells were used for experiments 48 h after initial virus exposure. siRNA ON-TARGETplus smart pools were used for genetic suppression in HBEC3-KT cells [Dharmacon: ANT1 (*SLC25A4*, #L-007485-00-0005), ANT2 (*SLC25A5*, #L-007486-02-0005), non-targeting control pool #D-001810-10-05] using Lipofectamine 2000 (Invitrogen) per manufacturer's instructions. Overexpression and targeted knockdown were confirmed with western analysis for each protein at 24, 48 and 72 h.

Cellular viability, metabolism and ATP measurements

For viability analysis, HBEC3-KT cells were cultured in 384-well glass bottom plates, and infected with adenovirus constructs for ANT1-GFP, ANT2-GFP and control GFP vector. At 48 h post-infection, cells were treated with keratinocyte serum-free medium (KSFM; Gibco, ThermoFisher) alone or 10–80% CSE for 24 h. Cells were stained with Alexa Fluor 405-conjugated Annexin V, ethidium homodimer (necrotic cells) (Biotium, Inc), and Draq5 (nuclei) for viability experiments or MitoSOX Red and Draq5 for oxidative stress analysis. Cells were washed once with binding buffer and imaged in L-15 Leibovitz medium on a Molecular Devices High Content imager using 20 \times and 60 \times objectives capturing four frames per well. Mitochondrial reactive oxygen species production was assessed using MitoSOX Red staining in cells treated with adenovirus and CSE as above. Cells were washed once with PBS and incubated with MitoSOX for 10 min at 37°C, 5% CO₂. Nuclei were labeled with Draq5 (#4084, Cell Signaling). Cells were washed three times with PBS and placed in L-15 Leibovitz medium for imaging using the High Content Imager. For cell analysis, fluorescence intensity of mitochondria was assessed with exclusion of the nucleus. Per well, 500–1700 cells were analyzed, eight wells per experiment on 2–3 different days. For cell analysis, MetaXpress software (Molecular Devices) was used to separate cells infected with adenovirus constructs from uninfected cells. The average fluorescence intensities of MitoSOX staining in mitochondria were determined with exclusion of the nucleus. Approximately 300–400 cells were analyzed per well for a total of 700–1500 cells per group. Across all replicates, 2800–4500 cells per group were evaluated.

The Seahorse XF Mito Stress assay (XF96 FluxAnalyzer, Agilent) was used for metabolic analysis of HBEC3-KT cells with ANT modulation. HBEC3-KT cells were cultured in 96-well Seahorse assay plates (Agilent) and infected with adenovirus constructs expressing ANT1 or ANT2 and

control for target overexpression at 48 h (MOI 40, Vector BioLabs) or siRNA-targeted suppression by using siRNA and Lipofectamine as described above for ANT1, ANT2 or non-targeting control siRNA at 72 h. After viral infection or siRNA transfection, cells were treated for 4 h with KSFM alone or 20% CSE. Cells were washed once in KSFM, followed by washes in buffered Seahorse Assay medium (pH 7.4) and subsequent metabolic testing according to the manufacturer's protocol (Agilent, Seahorse XF96). Oligomycin (2 μ M, ATPase inhibitor), FCCP (0.25 μ M mitochondrial uncoupler), and a cocktail of rotenone (0.5 μ M, ETC complex I inhibitor) and antimycin A (0.5 μ M, ETC complex III inhibitor) were sequentially injected after three basal rates were measured. Real-time oxygen consumption rate (OCR) is determined including basal OCR (before test kit inhibitors), maximal OCR (after FCCP treatment, a mitochondrial uncoupler), ATP production (OCR after injection of the complex V inhibitor oligomycin), and proton leak. Sample measurements were normalized to total cellular mass determined by CyQuant Assay according to the manufacturer's protocol (Molecular Probes, ThermoFisher). For experiments including ANT-specific inhibitors, carboxyatractyloside (CATR, 20 μ M, Sigma), bongkrekic acid (BKA, 4 μ M, Sigma), or PBS vehicle control were injected into wells after basal OCR measurements were taken, followed by repeat OCR measurements 30 min after compound injection. Cells were then analyzed according to the Seahorse assay protocol as described above.

Steady-state intracellular ATP concentrations were measured in HBEC3-KT cells after overexpression of adenoviral ANT1-GFP, ANT2-GFP, and GFP control for 48 h followed by treatment with medium alone or 20% CSE for 4 h. Cell lysates were collected with ATP lysis buffer supplemented with 300 μ M of ecto-ATPase inhibitor ARL 67156 (Sigma) by using a luciferin-luciferase bioluminescence ATP Determination Kit (ThermoFisher) with an ATP standard curve. The ATP concentration in mM/HBEC3-KT cell was calculated by considering the cellular volume of a single HBEC3-KT cell and the amount of ATP in a single cell as shown in the following equation: Amount of ATP per cell = (concentration of ATP per cell) \times (volume of cell).

Spherical cell volume was determined after measuring the diameter of trypsinized HBEC3-KT cells on an epifluorescence microscope (Olympus). The amount of ATP for one cell was derived from the amount of protein in one cell found by using Bradford assay (BioRad).

Measuring airway surface liquid height

Airway surface liquid (ASL) was visualized by adding 10 kD-Texas Red-dextran (ThermoFisher) to the apical surface of NHBE or HBEC3-KT cell cultures at ALI, as previously described (Amarante et al., 2014; Button et al., 2008; Lazarowski et al., 2004), and z-stack ASL images were collected 4 h later with a confocal microscope at 37°C, 5% CO₂. The apical surface of cells was washed once with PBS 18 h prior to the addition of Texas Red. ASL was visualized by adding 10 kD Texas Red-dextran (17.5 μ l per 12-well insert and 6.7 μ l per 24-well insert at 1.5 mg/ml in sterile PBS, ThermoFisher) to the apical surface of NHBE or HBEC3-KT cell cultures at ALI, as previously described (Amarante et al., 2014; Button et al., 2008; Lazarowski et al., 2004). Fluorinert (100 μ l per 12-well insert and 30 μ l per 24-well insert) was added to the top of the insert cultures to prevent evaporation. ASL was imaged 4 h later by acquiring 3 \times 3 or 4 \times 4 tiled z-stacks by live-cell confocal microscopy with a heat and CO₂-controlled stage (Zeiss 780 or Nikon A1R confocal microscope with a 40 \times water objective). z-stack images at the ASL were captured at 0.46 μ m step size, and analyzed by segmentation and pixel thickness analysis. For experiments with ANT inhibitors, CATR (20 μ M, Sigma) and BKA (4 μ M, Sigma) in PBS (or control PBS alone) were added to the Texas Red-dextran dye and applied to the apical surface of ALI cultures (NHBE or HBEC3-KT cells) 4 h prior to ASL assessment. For apyrase treatment, 10 units of apyrase (Sigma) was added with Texas Red-dextran 4 h prior to ASL assessment, as described above.

Thickness across the sample was computed using a custom script, written in Matlab (MathWorks, Natick, MA). Briefly, for each value x in the three-dimensional images, $\text{Im}(x, y, z)$, the resultant (y, z) slice was segmented using adaptive thresholding (Matlab command: `imbinarize`), followed by operations to fill holes (`imfill`), morphological opening (`imopen`) and filtering of small regions (`bwareopen`) (Fig. S4D). The threshold level was adjusted after preprocessing the complete image and the process repeated.

For each y in this binary image, the number of segmented pixels was counted, giving a measure of the thickness in the (x, y) location; see Fig. S1. This gave a histogram of depths over the image (Fig. S4E,F). An average depth was computed for all pixels in which a non-zero depth was detected (to avoid edge effects). The process was repeated by fixing y and working with the (x, z) slice. The differences between the averages were typically less than 1–2%. Thickness in pixels was converted to μ m using a slice thickness of 0.46 μ m, the step size used to collect the z-stack.

Ciliary beat frequency

Ciliary beat frequency (CBF) was assessed at 48 h post-adenoviral infection. Inserts were imaged in a 12-well Falcon plate with buffered L-15 Leibovitz medium (Gibco) and imaged within 2 min of placement. Bright-field images of beating cilia were captured at 160 frames/s over 4 s (3–5 videos per insert, Leica Spinning disc confocal with 40 \times water objective). For air or cigarette smoke experiments, 'pre-treatment' images ($n=3$ per insert) were captured at random insert locations followed by exposure to air or cigarette smoke by the Vitrocell system (2 cigarettes over 16 min). 'Post-treatment' images were collected at similar locations on each insert 30 min after the treatment. Cells were kept in ALI growth medium at 37°C and 5% CO₂ when not being imaged. Cells were 'rested' for 4 h and imaged again ($n=3$ videos per insert). Beat frequency analysis was completed using a Matlab script assessing pixel intensity fluctuations (Fig. S4G–J). CBF data were compared with SAVA analysis (Sisson et al., 2003) and both outputs agreed closely.

A custom script, written in Matlab, was used to estimate the beating frequency of cilia. Individual images from a video consisting of N frames were used to create a three-dimensional matrix $\text{Im}_k(x, y)$, where (x, y) denotes location in the image of each pixel, and $k \in 1, \dots, n$ is the frame number. For each (x, y) , the corresponding sequence of intensities was first normalized using:

$$p_{ij}(k) = \frac{\text{Im}_k(x, y) - \min_k \text{Im}_k(x, y)}{\max_k \text{Im}_k(x, y) - \min_k \text{Im}_k(x, y)},$$

so, that $0 \leq p_{ij}(k) \leq 1$ and filtered by removing the mean value:

$$\tilde{p}_{ij}(k) = p_{ij}(k) - \frac{1}{N} \sum_{k=1}^N p_{ij}(k).$$

The Fast-Fourier transform (FFT) of $\sim p_{ij}(k)$ was obtained using the Matlab command `fft`:

$$q_{ij}(n) = \sum_{k=1}^N \tilde{p}_{ij}(k) e^{-2\pi i n k / N}, \quad n = 0, \dots, N-1.$$

The corresponding single-sided power spectrum was computed by using:

$$\tilde{q}_{ij}(n) = \begin{cases} |q_{ij}(0)|, & n = 0 \\ 2|q_{ij}(n)|, & n = 1, \dots, N/2 \end{cases}$$

where N is even, giving a power spectrum for each pixel (see Fig. S4H,I).

To determine the frequency of beating, we carried out two approaches. In the first, we found the frequency with highest power density for each of the pixels. We then used a threshold of 0.125 arbitrary units (A.U.) to determine whether there was any detectable power in that pixel or not. The frequency with highest power was determined, and these data were aggregated over all pixels meeting this threshold (Fig. S4I). The data between 2 Hz and 20 Hz of the corresponding histogram were then normalized and fit by a single Gaussian function, $\alpha \exp^{-(f-\mu)/\sigma^2}$, where f is the frequency, using the `fit` command. The mean (μ) of the distribution was used as a measure of beating frequency. The parameter σ is equal to $\sqrt{2} \times$ standard deviation and denotes the tightness of this distribution. Parameter α serves as a normalization factor. The percent of all pixels in this frequency range is reported in Fig. 5C.

In the second method, we aggregated the power spectra from all pixels (without thresholding): $\bar{q}(n) = \sum_{ij} \tilde{q}_{ij}(n)$, and fit the data between 2 Hz and 20 Hz to a Gaussian mixture model using three modes (Fig. S4J). This

resultant μ value with the greatest contribution to the mixture model was used. Both methods provided similar estimates, so the data reported used the first method described above.

Animal studies

Mouse smoke exposure and processing

All animal experiments were performed in accordance with the Institutional Animal Care and Use Committee (IACUC) of the University of Pittsburgh. Animals were housed according to standard housing criteria. C57Bl/6J mice (female mice at 10 weeks of age, $n=5$ per group) were subjected to the smoke of four unfiltered cigarettes per day (lot number 1R5F; University of Kentucky, Lexington, KY), 5 days a week for a duration of 6 months, using a smoking apparatus that delivers targeted cigarette smoke to single mice isolated in individual chambers (Hautamaki et al., 1997). The controls in each group were exposed to room-air alone. These mice were caged separately and housed in the same facility as their smoke-exposed counterparts. At the completion of each experiment, mice were killed by CO₂ inhalation, the chest was opened, and the trachea cannulated. Lungs were inflated with 10% buffered formalin at a constant pressure of 25 cm H₂O for 15 min. The lungs were then ligated, excised and fixed in formalin for 24 h before embedding in paraffin. Serial midsagittal sections were obtained for histological analysis. In a subset of animals, lungs did not undergo fixation and instead were excised and placed directly in liquid nitrogen for RNA isolation. Whole-lung RNA was isolated using Trizol per the manufacturer's (Invitrogen) protocol.

Human tissue studies

Studies using human tissues were approved by the University of Pittsburgh and Johns Hopkins Institutional Review Boards (McElvaney et al., 1989) in accordance with ethical guidelines. For immunohistochemical studies, donor human lung tissue (control and COPD patients) was attained and approved through the National Heart, Lung, and Blood Institute's Lung Tissue Research Consortium database and the Center for Organ Recovery and Education (CORE) at the University of Pittsburgh (Lennox et al., 2018; Myerburg et al., 2010). Human lung tissues used for real-time PCR were obtained from explanted lungs after lung transplantation or donor lungs unsuitable for organ transplantation (The Airway Cell and Tissue Core, supported by P30 DK072506, NIDDK and the CFF RDP to the University of Pittsburgh). Lung tissues were stored at -80°C until future usage.

Human and mouse lung tissue mRNA expression

Human lung tissue from The Airway Cell and Tissue Core at the University of Pittsburgh (Control and COPD lung) was homogenized in Trizol, total RNA was isolated according to the manufacturer's instructions (Thermo Fisher, Grand Island, NY) and RNA was reverse-transcribed (Applied Biosystems, Grand Island, NY). Real time PCR was performed using total cDNA and primer pairs flanking introns specifically targeted the genes of interest (*slc25a4*, *slc25a5*, and *ACTB*) using Sybr green master mix for real time PCR (Applied Biosystems, Grand Island, NY). Real time PCR primer pairs included *slc25a4*, forward 5'-TGGATGATTGCCAGAGTGT-3' and reverse 5'-GGCTCCTTCGTCTTTTGCAA-3'; *slc25a5*, forward 5'-GGCTTTAACGTGTCTGTGCA-3' and reverse 5'-ATAGGAAGTCAAC-CCGGCAA-3'; *slc25a6*, forward 5'-ACGCCCTCCATTCACTCTC-3' and reverse 5'-GCTTGACCCGCTCGATCG-3'; *slc25a31*, forward 5'-TTCC-GCTTCCCTTCATCGTA-3' and reverse 5'-GCCACCGCTGTCTTGGAC-3'; *ACTB*, forward 5'-ATCCGCCGCCCGTCC-3' and reverse 5'-CGAT-GGAGGGGAAGACGG-3'. Each sample was measured in quadruplicate. A single technical outlier was removed from samples with technical standard deviation (s.d.) >1 , individual samples were excluded if removal of an outlier failed to reduce technical s.d. <1 in either the gene of interest or the housekeeping gene. The relative fold change was calculated by normalizing to β -actin and comparing between lung tissue from individuals with a history of COPD and those without a history of COPD using the $\Delta\Delta\text{CT}$ method. The error was calculated as a positive or negative error = $2^{\pm[\text{fold change} \pm \sqrt{(\text{s.e.m. of } ACTB^2 + \text{s.e.m. of gene}^2)}]}$.

For mouse lung tissues and human ALI cultures on inserts, total RNA was extracted using Trizol with analysis by real-time PCR according to manufacturer's instructions (One-step VERSO SYBR green PCR kit, Thermo Fisher Scientific). Total RNA was extracted from mouse lung tissue

using Trizol with analysis of 25 ng of RNA reverse transcribed and complementary DNA was amplified by real-time-PCR using a One-step VERSO SYBR green PCR kit (Thermo Fisher Scientific) on a BioRad CFX96 Real-Time PCR machine. The PCR protocol included cDNA synthesis 50°C for 15 min followed by repeat cycles of inactivation at 95°C for 15 min, denaturing of DNA at 95°C for 15 s, annealing at 60°C for 30 s, extension at 72°C for 30 s (repeat for a total of 40 cycles). PCR primer efficiency was determined, amplicon melting curves (60 – 95°C) and single product of correct size by gel analysis were determined to verify production of single amplicons. No template and no enzyme controls were compared. Target primers were used at 200 nM and include: Sigma KiQ primer sets for mouse *slc25a4*/ANT1 (#M_Slc25a4_1) and mouse *slc25a5*/ANT2 (#M_Slc25a5_1). Other primers include mouse GAPDH, human *slc25a4*/ANT1 (forward 5'-TGGATGATTGCCAGAGTGT-3'; reverse 5'-GGC-TCCTTCGTCTTTTGCAA-3'). Targeted Taqman FAM probe sets included human MUC5ac (Hs01365616_m1), MUC5B (Hs008615595_m1) and GAPDH (Hs02786624_g1) from ThermoFisher. The real-time PCR data were analyzed by the $\Delta\Delta\text{CT}$ method with normalization to GAPDH and comparing smoke-exposed mouse lung tissue to air-exposed controls.

Human microarray data

Microarray data were analyzed from the Lung Genome Research Consortium (LGRC, University of Pittsburgh) and using the publicly available Geo Omnibus Data set, GDS2486 previously published (Harvey et al., 2007; Tilley et al., 2009). The LGRC data set is a genome-wide association study of human whole lung tissue mRNA from control individuals ($n=137$) and those with COPD ($n=219$). The Geo Omnibus Data set GDS2486, previously published (Harvey et al., 2007; Tilley et al., 2009) and publicly available, includes Affymetrix analysis (Affymetrix Human Genome U133 Plus 2.0 Array) of human small airway epithelial cell brushings from non-smokers ($n=12$) versus smokers ($n=10$). Data were analyzed *a priori* for gene expression of *SLC25A4*/ANT1 and *SLC25A5*/ANT2 with normalization to glucose-6-phosphate isomerase (GPI). Gene expression data do not represent multivariate comparisons and statistical analysis was completed using a Kruskal–Wallis followed by pairwise Mann–Whitney test with $P<0.05$ considered to be statistically significant. For this analysis, subjects were stratified by COPD severity as defined by the 2007 global initiative of obstructive lung disease (GOLD) classification, i.e. 1, mild; 2, moderate; 3, severe; 4, very severe (Rabe et al., 2007).

Human protein expression

Immunoblot analysis was completed on cell culture protein lysates, yeast *S. cerevisiae* protein lysates, or mouse lung tissue homogenates. Mammalian cell culture lysates were attained using RIPA buffer with protease inhibitor cocktails I, II and III (Sigma), RNase, and 150 nM aprotinin. Yeast protein lysates were obtained from yeast expressing human ANT1–4 ($\Delta\text{aac}[EV]$, $\Delta\text{aac}[ANT1]$, $\Delta\text{aac}[ANT2]$, $\Delta\text{aac}[ANT3]$, $\Delta\text{aac}[ANT4]$, OD₆₀₀=3 per group) via alkaline lysis with NaOH/ β -mercaptoethanol and trichloroacetic acid. Protein concentration was determined by Bradford Assay (Pierce). Proteins were resolved by 10–15% SDS-polyacrylamide gel electrophoresis and transferred to a nitrocellulose membrane. Proteins of interest were immunoblotted using primary antibodies (incubated overnight at 4°C) followed by detection with Li-Cor secondary fluorophore conjugated antibodies using a Li-Cor Odyssey CLx. GAPDH and Ponceau S membrane staining were used as protein loading controls. Antibodies that recognize the following proteins were used (dilutions, source and species are listed in parentheses): human ANT1 [1:500, ab1F3H11 made in the laboratory of S.M.C. (Lu et al., 2017), mouse], ANT2 [1:500, ab5H7, from S.M.C. (Jones et al., 1992), mouse], TOM20 (1:1000, Abcam #ab186734, rabbit monoclonal), GAPDH (1:1000, Life Technologies A6455, rabbit). Antibody 1F3H11 for ANT1 (paralog specific) only worked for western analysis.

Human/mouse immunohistochemistry and immunocytochemistry

Mouse lungs were inflation fixed with 10% buffered formalin at a constant pressure of 25 cm H₂O for 10 min. The lungs were then ligated, excised and fixed in formalin for 24 h before washing for 10 min in PBS and embedding in paraffin. Serial mid-sagittal sections were obtained for histological

analysis. Fresh frozen and formalin fixed paraffin embedded human lungs were also stained from normal case controls and COPD patients. Sections were cut at 5–7 μm and were adhered to slides for 60 min at 60°C followed by deparaffination with xylene and rehydration in an ethanol series (for paraffin tissues). The sections were treated with sodium citrate buffer pH 6.0 at 95°C for antigen retrieval. Antigen retrieval for TOM20 and COX4 antibodies in human lung tissue was completed using Tris-EDTA buffer, pH 9.0 at 95°C for 20 min. Human and mouse lung sections were stained for colocalization with primary and secondary antibodies: ANT1 (Abcam #ab102032 rabbit polyclonal, 1:1000), pan ANT (anti-ANT1/2/3 Abcam, #ab110322, mouse monoclonal 1:100), ANT2 (SH7, from S.M.C., 1:100), ANT2 (Abcam, #ab118076, mouse monoclonal, 1:100), ANT2 (Abcam, #ab222843, 1:1000), ANT2/3 (Abcam, #ab230545, 1:100), acetylated α -tubulin (Cell Signaling, #5335T Rabbit at 1:2000 and Invitrogen, #32-2700 Mouse at 1:2000), TOM20 (Abcam, mouse #ab56783 and Cell Signaling, rabbit #42406S), COX4-Alexa Fluor 488 (Cell Signaling, #4853S, 1:200), GFP (Aves Labs Inc, 1:1000), goat anti-mouse, anti-rabbit or anti-chicken Alexa Fluor 488, 555 and 647 (Molecular Probes). Antibodies used for each experiment are designated in the figures. Images were captured on a Zeiss 780 confocal microscope with an iPlan Apochromat 63 \times /1.4 NA oil objective, on a Nikon A1R with 60 \times objective or Nikon SIM microscope using a 100 \times objective with SIM reconstruction after image capture. Control sections were stained with non-immune rabbit IgG (#2729P, Cell Signaling). Quantification of ANT staining was determined by making regions of interest (Vestbo et al. 2013) of the ciliary region with a second ROI with the associated mitochondrial area below that layer (see Figs S6B and S7B). Approximately 5–14 measurements were made per ciliated area of epithelium per image. Mean pixel intensities were normalized to background by subtracting the mean pixel intensity for a large background ROI. The sum was calculated separately for the ROI areas and ROI normalized mean intensities for the ciliary and mitochondrial areas. The integrated intensity was calculated by dividing the sum of the ROI normalized mean intensities by the sum of the ROI areas. Images with multiple colors are displayed with each channel in grayscale for clarity and a composite pseudocolor image.

For immunocytochemistry on cells in culture on glass or on inserts at ALI, cells were fixed in fresh 4% paraformaldehyde for 10 min at 4°C. For select experiments to label mitochondria, cells were incubated with Mitotracker Deep Red (Invitrogen, #M22426) for 20 min at 37°C according to manufacturer's protocol followed by PFA fixation. Cells were washed three times in PBS, permeabilized with ice-cold 0.3% Triton X-100 with 1% BSA in PBS for 10 min followed by three washes in PBS. To prevent non-specific staining, cells were blocked with 2% BSA in PBS for 45 min at room temperature. Cells were washed five times with 0.5% BSA in PBS. Cells were incubated with primary antibody overnight at 4°C followed by five washes with 0.5% BSA in PBS. Cells were incubated with secondary antibody dilutions (made in 0.5% BSA in PBS) for 60 min at room temperature in the dark. Cells are washed 5 times with 0.5% BSA in PBS followed by five PBS washes. Nuclei were stained with Hoechst at 10 $\mu\text{g}/\text{ml}$ for 10 min followed by PBS washes. For insert staining, insert membranes are cut out and placed apical surface upright onto glass slides. Sections were mounted in Prolong Diamond Antifade Mounting Agent (Molecular Probes, ThermoFisher), cured for at least 24 h at room temperature, and sealed with clear nail polish. Samples were stored at 4°C protected from light for long-term storage. To assess the membrane localization of ANT proteins that use differential permeabilization, ALI cultured cells were blocked as above, incubated with the noted primary antibody against ANT with subsequent washes, followed by 1 h incubation with secondary antibody conjugated to Alexa Fluor 555 all without permeabilization. Then, the tissues were permeabilized and incubated again with the same primary antibody against ANT1 or ANT2/3 proteins as noted in the figure labels for 2 h at room temperature, washed and incubated for 1 h with secondary antibody conjugated to Alexa Fluor 488. The remaining processing was similar for subsequent confocal imaging.

Molecular phylogenetic tree analysis

The evolutionary history was inferred by using the Maximum Likelihood method based on the JTT matrix-based model (Jones et al., 1992). The

bootstrap consensus tree inferred from 500 replicates (Felsenstein, 1985) is taken to represent the evolutionary history of the taxa analyzed. Branches corresponding to partitions reproduced in <50% bootstrap replicates are collapsed. The percentage of replicate trees in which the associated taxa clustered together in the bootstrap test (500 replicates) is shown in red next to the branches (Felsenstein, 1985). Initial tree(s) for the heuristic search were obtained automatically by applying Neighbor-Join and BioNJ algorithms to a matrix of pairwise distances estimated using a JTT model, and then selecting the topology with superior log likelihood value. The tree is drawn to scale, with branch lengths measured in the number of substitutions per site. The analysis involved 22 amino acid sequences. All positions containing gaps and missing data were eliminated. There was a total of 289 positions in the final dataset. Evolutionary analyses were conducted in MEGA7 (Kumar et al., 2016).

Quantification and statistical analysis

Mean densitometry and all other quantitative data (mean \pm s.e.m.) are normalized to appropriate control groups and assessed for normalcy. If the samples are normally distributed, then the data sets are analyzed for significance using ANOVA followed by a Fisher's least significant difference (LSD) post hoc test. When data are not normally distributed, nonparametric analyses, including Kruskal–Wallis and/or Mann–Whitney were used.

Key Reagents and Materials

A complete list of key resources is given in Table S1. The document includes information on the following: antibodies; bacterial, yeast and viral strains; biological samples; chemicals, peptides and recombinant proteins; critical commercial assays and equipment; deposited data; experimental models, including organisms and strains; oligonucleotides; recombinant DNA and siRNA; MatLab Scripts; and other resources.

Acknowledgements

We thank the University of Pittsburgh Lung Tissue and Airway Cell Core funded by the CF Foundation Research Development Grant (J. Pilewski and M. Myerburg), Randal Reed (Johns Hopkins University) for mouse nasal epithelial tissue sections, Carolyn Machamer (Johns Hopkins University) for helpful discussions and Corinne Sandone (Johns Hopkins University) for the artwork in Figs 1 and 8. We thank members of the D.N.R.'s lab (Johns Hopkins) and Steve Shapiro (University of Pittsburgh) for helpful comments on the manuscript. We thank Dr Douglas Wallace, Children's Hospital of Pennsylvania for the ANT1 knockout mice. We thank the University of Pittsburgh Center for Biological Imaging (S. Watkins and C. St. Croix) and the Johns Hopkins Institute for Basic Biomedical Sciences Microscope Facility for imaging assistance (Confocal Instrument grant NIH S10OD016374).

Competing interests

The authors declare no competing or financial interests.

Author contributions

Conceptualization: C.R.K., S.M.C., V.K.S., D.N.R.; Methodology: C.R.K., J.M.N., M.K., Y.L., V.K.S., D.N.R.; Software: P.A.I.; Validation: C.R.K., J.M.N., M.K., P.A.I., D.N.R.; Formal analysis: C.R.K., J.M.N., J.E.R., P.A.I., D.N.R.; Investigation: C.R.K., J.M.K.N., M.K., Y.L., J.E.R., A.D.G.; Resources: C.R.K., S.M.C., F.C.S., Y.Z., A.D.G., V.K.S., D.N.R.; Data curation: C.R.K., F.C.S., Y.Z.; Writing - original draft: C.R.K.; Writing - review & editing: C.R.K., J.M.K.N., S.M.C., V.K.S., D.N.R.; Visualization: C.R.K., D.N.R.; Supervision: C.R.K., D.N.R.; Project administration: C.R.K., D.N.R.; Funding acquisition: C.R.K., D.N.R.

Funding

We thank the National Institutes of Health (NIH): National Heart, Lung, and Blood Institute (NHLBI) (F32HL129660 and K08HL141595 to C.R.K.; R01HL124099 to R.S. and D.N.R.; R01HL108882 to S.M.C.); National Institute of General Medical Sciences (NIGMS) (R01GM66817 to D.N.R.); Other funding was obtained through a Biochemistry, Cellular, and Molecular Biology Program Training Grant T32GM007445 (to Y.L.); the Burroughs Wellcome Fund CAMs Award, Parker B Francis Pulmonary Fellowship, and Johns Hopkins Bauernschmidt Fellowship Foundation (to C.R.K.); the Thomas Wilson Foundation (to D.N.R.); the American Heart Association (12PRE11910004 to Y.L.); and the Airway Cell and Tissue Core supported by P30 DK072506 (Mike Meyerberg), the National Institute of Diabetes and Digestive and Kidney Diseases (NIDDK) and the CFF RDP (to Y.Z.).

at the University of Pittsburgh) for funding support. Deposited in PMC for release after 12 months.

Supplementary information

Supplementary information available online at
<https://jcs.biologists.org/lookup/doi/10.1242/jcs.257162.supplemental>

Peer review history

The peer review history is available online at
<https://jcs.biologists.org/lookup/doi/10.1242/jcs.257162.reviewer-comments.pdf>.

References

- Amarante, T. D., da Silva, J. K. L. and Garcia, G. J. M. (2014). Effects of airway surface liquid height on the kinetics of extracellular nucleotides in airway epithelia. *J. Theor. Biol.* **363**, 427–435. doi:10.1016/j.jtbi.2014.08.030
- Astrand, A. B. M., Hemmerling, M., Root, J., Wingren, C., Pesic, J., Johansson, E., Garland, A. L., Ghosh, A. and Tarran, R. (2015). Linking increased airway hydration, ciliary beating, and mucociliary clearance through ENaC inhibition. *Am. J. Physiol. Lung Cell. Mol. Physiol.* **308**, L22–L32. doi:10.1152/ajplung.00163.2014
- Bustamante-Marin, X. M. and Ostrowski, L. E. (2017). Cilia and mucociliary clearance. *Cold Spring Harb. Perspect. Biol.* **9**, a028241. doi:10.1101/cshperspect.a028241
- Button, B. and Boucher, R. C. and University of North Carolina Virtual Lung Group (2008). Role of mechanical stress in regulating airway surface hydration and mucus clearance rates. *Respir. Physiol. Neurobiol.* **163**, 189–201. doi:10.1016/j.resp.2008.04.020
- Button, B., Okada, S. F., Frederick, C. B., Thelin, W. R. and Boucher, R. C. (2013). Mechanosensitive ATP release maintains proper mucus hydration of airways. *Sci. Signal.* **6**, ra46. doi:10.1126/scisignal.2003755
- Cardouat, G., Duparc, T., Fried, S., Perret, B., Najib, S. and Martinez, L. O. (2017). Ectopic adenine nucleotide translocase activity controls extracellular ADP levels and regulates the F1-ATPase-mediated HDL endocytosis pathway on hepatocytes. *Biochim. Biophys. Acta Mol. Cell Biol. Lipids* **1862**, 832–841. doi:10.1016/j.bbalip.2017.05.005
- Clunes, L. A., Davies, C. M., Coakley, R. D., Aleksandrov, A. A., Henderson, A. G., Zeman, K. L., Worthington, E. N., Gentzsch, M., Kreda, S. M., Cholon, D. et al. (2012). Cigarette smoke exposure induces CFTR internalization and insolubility, leading to airway surface liquid dehydration. *FASEB J.* **26**, 533–545. doi:10.1096/fj.11-192377
- Dvorak, A., Tilley, A. E., Shaykhiev, R., Wang, R. and Crystal, R. G. (2011). Do airway epithelium air-liquid cultures represent the in vivo airway epithelium transcriptome? *Am. J. Respir. Cell Mol. Biol.* **44**, 465–473. doi:10.1165/rcmb.2009-0453OC
- Elliott, M. K., Sisson, J. H. and Wyatt, T. A. (2007). Effects of cigarette smoke and alcohol on ciliated tracheal epithelium and inflammatory cell recruitment. *Am. J. Respir. Cell Mol. Biol.* **36**, 452–459. doi:10.1165/rcmb.2005-0440OC
- Esposito, L. A., Melov, S., Panov, A., Cottrell, B. A. and Wallace, D. C. (1999). Mitochondrial disease in mouse results in increased oxidative stress. *Proc. Natl. Acad. Sci. USA* **96**, 4820–4825. doi:10.1073/pnas.96.9.4820
- Felsenstein, J. (1985). Confidence limits on phylogenies: An approach using the bootstrap. *Evolution* **39**, 783–791. doi:10.1111/j.1558-5646.1985.tb00420.x
- Ghosh, A., Boucher, R. C. and Tarran, R. (2015). Airway hydration and COPD. *Cell. Mol. Life Sci.* **72**, 3637–3652. doi:10.1007/s00018-015-1946-7
- Graham, B. H., Waymire, K. G., Cottrell, B., Trownc, I. A., MacGregor, G. R. and Wallace, D. C. (1997). A mouse model for mitochondrial myopathy and cardiomyopathy resulting from a deficiency in the heart/muscle isoform of the adenine nucleotide translocator. *Nat. Genet.* **16**, 226–234. doi:10.1038/ng0797-226
- Harvey, B.-G., Heguy, A., Leopold, P. L., Carolan, B. J., Ferris, B. and Crystal, R. G. (2007). Modification of gene expression of the small airway epithelium in response to cigarette smoking. *J. Mol. Med. (Berl.)* **85**, 39–53. doi:10.1007/s00109-006-0103-z
- Hautamaki, R. D., Kobayashi, D. K., Senior, R. M. and Shapiro, S. D. (1997). Requirement for macrophage elastase for cigarette smoke-induced emphysema in mice. *Science* **277**, 2002–2004. doi:10.1126/science.277.5334.2002
- Hoffmann, R. F., Zarrintan, S., Brandenburg, S. M., Kol, A., de Bruin, H. G., Jafari, S., Dijk, F., Kalicharan, D., Kelders, M., Gosker, H. R. et al. (2013). Prolonged cigarette smoke exposure alters mitochondrial structure and function in airway epithelial cells. *Respir. Res.* **14**, 97. doi:10.1186/1465-9921-14-97
- Hoshino, A., Wang, W. J., Wada, S., McDermott-Roe, C., Evans, C. S., Gosis, B., Morley, M. P., Rath, K. S., Li, J., Li, K. et al. (2019). The ADP/ATP translocase drives mitophagy independent of nucleotide exchange. *Nature* **575**, 375–379. doi:10.1038/s41586-019-1667-4
- Jastroch, M., Divakaruni, A. S., Mookerjee, S., Treberg, J. R. and Brand, M. D. (2010). Mitochondrial proton and electron leaks. *Essays Biochem.* **47**, 53–67. doi:10.1042/bse0470053
- Jones, D. T., Taylor, W. R. and Thornton, J. M. (1992). The rapid generation of mutation data matrices from protein sequences. *Comput. Appl. Biosci.* **8**, 275–282. doi:10.1093/bioinformatics/8.3.275
- Kim, H. S., Je, J. H., Son, T. G., Park, H. R., Ji, S. T., Pokharel, Y. R., Jeon, H. M., Kang, K. W., Kang, H. S., Chang, S. C. et al. (2012). The hepatoprotective effects of adenine nucleotide translocator-2 against aging and oxidative stress. *Free Radic. Res.* **46**, 21–29. doi:10.3109/10715762.2011.636042
- Klumpe, I., Savvatis, K., Westermann, D., Tschöpe, C., Rauch, U., Landmesser, U., Schultheiss, H.-P. and Dörner, A. (2016). Transgenic overexpression of adenine nucleotide translocase 1 protects ischemic hearts against oxidative stress. *J. Mol. Med. (Berl.)* **94**, 645–653. doi:10.1007/s00109-016-1413-4
- Kokoszka, J. E., Waymire, K. G., Flierl, A., Sweeney, K. M., Angelin, A., MacGregor, G. R. and Wallace, D. C. (2016). Deficiency in the mouse mitochondrial adenine nucleotide translocator isoform 2 gene is associated with cardiac noncompaction. *Biochim. Biophys. Acta* **1857**, 1203–1212. doi:10.1016/j.bbabi.2016.03.026
- Kretova, M., Sabova, L., Hodny, Z., Bartek, J., Kollarovic, G., Nelson, B. D., Hubackova, S. and Luciaková, K. (2014). TGF- β /NF1/Smad4-mediated suppression of ANT2 contributes to oxidative stress in cellular senescence. *Cell. Signal.* **26**, 2903–2911. doi:10.1016/j.cellsig.2014.08.029
- Kumar, S., Stecher, G. and Tamura, K. (2016). MEGA7: molecular evolutionary genetics analysis Version 7.0 for bigger datasets. *Mol. Biol. Evol.* **33**, 1870–1874. doi:10.1093/molbev/msw054
- Lazarowski, E. R. and Harden, T. K. (1999). Quantitation of extracellular UTP using a sensitive enzymatic assay. *Br. J. Pharmacol.* **127**, 1272–1278. doi:10.1038/sj.bjp.0702654
- Lazarowski, E. R., Tarran, R., Grubb, B. R., van Heusden, C. A., Okada, S. and Boucher, R. C. (2004). Nucleotide release provides a mechanism for airway surface liquid homeostasis. *J. Biol. Chem.* **279**, 36855–36864. doi:10.1074/jbc.M405367200
- Lazarowski, E. R., Sesma, J. I., Seminario, L., Esther, C. R., Jr and Kreda, S. M. (2011). Nucleotide release by airway epithelia. *Subcell. Biochem.* **55**, 1–15. doi:10.1007/978-94-007-1217-1_1
- Lennox, A. T., Coburn, S. L., Leech, J. A., Heidrich, E. M., Kleymann, T. R., Wenzel, S. E., Pilewski, J. M., Corcoran, T. E. and Myerburg, M. M. (2018). ATP12A promotes mucus dysfunction during Type 2 airway inflammation. *Sci. Rep.* **8**, 2109. doi:10.1038/s41598-018-20444-8
- Leopold, P. L., O'Mahony, M. J., Lian, X. J., Tilley, A. E., Harvey, B. G. and Crystal, R. G. (2009). Smoking is associated with shortened airway cilia. *PLoS ONE* **4**, e8157. doi:10.1371/journal.pone.0008157
- Liu, Y. and Chen, X. J. (2013). Adenine nucleotide translocase, mitochondrial stress, and degenerative cell death. *Oxid. Med. Cell Longev* **2013**, 146860. doi:10.1155/2013/146860
- Lu, Y. W., Acoba, M. G., Selvaraju, K., Huang, T. C., Nirujogi, R. S., Sathe, G., Pandey, A. and Claypool, S. M. (2017). Human adenine nucleotide translocases physically and functionally interact with respirasomes. *Mol. Biol. Cell* **28**, 1401–1589. doi:10.1091/mbc.e17-03-0195
- Lynn, E. G., Stevens, M. V., Wong, R. P., Carabenciov, D., Jacobson, J., Murphy, E. and Sack, M. N. (2010). Transient upregulation of PGC-1 α diminishes cardiac ischemia tolerance via upregulation of ANT1. *J. Mol. Cell. Cardiol.* **49**, 693–698. doi:10.1016/j.jmcc.2010.06.008
- Ma, H. P., Saxena, S. and Warnock, D. G. (2002). Anionic phospholipids regulate native and expressed epithelial sodium channel (ENaC). *J. Biol. Chem.* **277**, 7641–7644. doi:10.1074/jbc.C100737200
- Maestrelli, P., Sassetta, M., Mapp, C. E. and Fabbri, L. M. (2001). Remodeling in response to infection and injury. Airway inflammation and hypersecretion of mucus in smoking subjects with chronic obstructive pulmonary disease. *Am. J. Respir. Crit. Care. Med.* **164**, S76–S80. doi:10.1164/ajrcm.164.supplement_2.2106067
- Martinez, L. O., Najib, S., Perret, B., Cabou, C. and Lichtenstein, L. (2015). Ecto-F1-ATPase/P2Y pathways in metabolic and vascular functions of high density lipoproteins. *Atherosclerosis* **238**, 89–100. doi:10.1016/j.atherosclerosis.2014.11.017
- McElvaney, G., Blackie, S., Morrison, N. J., Wilcox, P. G., Fairbairn, M. S. and Pardy, R. L. (1989). Maximal static respiratory pressures in the normal elderly. *Am. Rev. Respir. Dis.* **139**, 277–281. doi:10.1164/ajrcm/139.1.277
- Murphy, S. L., Xu, J., Kochanek, K. D. and Arias, E. (2018). Mortality in the United States, 2017. *NCHS Data Brief.* **328**, 1–8.
- Myerburg, M. M., Harvey, P. R., Heidrich, E. M., Pilewski, J. M. and Butterworth, M. B. (2010). Acute regulation of the epithelial sodium channel in airway epithelia by proteases and trafficking. *Am. J. Respir. Cell Mol. Biol.* **43**, 712–719. doi:10.1165/rcmb.2009-0348OC
- Okada, S. F., Nicholas, R. A., Kreda, S. M., Lazarowski, E. R. and Boucher, R. C. (2006). Physiological regulation of ATP release at the apical surface of human airway epithelia. *J. Biol. Chem.* **281**, 22992–23002. doi:10.1074/jbc.M603019200
- Pan, S., Wang, N., Bisetto, S., Yi, B. and Sheu, S. S. (2015). Downregulation of adenine nucleotide translocator 1 exacerbates tumor necrosis factor- α -mediated cardiac inflammatory responses. *Am. J. Physiol. Heart Circ. Physiol.* **308**, H39–H48. doi:10.1152/ajpheart.00330.2014
- Rabe, K. F., Hurd, S., Anzueto, A., Barnes, P. J., Buist, S. A., Calverley, P., Fukuchi, Y., Jenkins, C., Rodriguez-Roisin, R., van Weel, C. et al. (2017). Global strategy for the diagnosis, management, and prevention of chronic

- obstructive pulmonary disease: GOLD executive summary. *Am. J. Respir. Crit. Care Med.* **176**, 532–555. doi:10.1164/rccm.200703-456SO
- Radojkovic, C., Genoux, A., Pons, V., Combes, G., de Jonge, H., Champagne, E., Rolland, C., Perret, B., Collet, X., Tercé, F. et al.** (2009). Stimulation of cell surface F1-ATPase activity by apolipoprotein A-I inhibits endothelial cell apoptosis and promotes proliferation. *Arterioscler. Thromb. Vasc. Biol.* **29**, 1125–1130. doi:10.1161/ATVBAHA.109.187997
- Raman, M., Sergeev, M., Garnaas, M., Lydeard, J. R., Huttlin, E. L., Goessling, W., Shah, J. V. and Harper, J. W.** (2015). Systematic proteomics of the VCP-UBXD adaptor network identifies a role for UBXN10 in regulating ciliogenesis. *Nat. Cell Biol.* **17**, 1356–1369. doi:10.1038/ncb3238
- Ramirez, R. D., Sheridan, S., Girard, L., Sato, M., Kim, Y., Pollack, J., Peyton, M., Zou, Y., Kurie, J. M., Dimaio, J. M. et al.** (2004). immortalization of human bronchial epithelial cells in the absence of viral oncoproteins. *Cancer Res.* **64**, 9027–9034. doi:10.1158/0008-5472.CAN-04-3703
- Robinson, D. N. and Spudich, J. A.** (2000). Dynacortin, a genetic link between equatorial contractility and global shape control discovered by library complementation of a Dictyostelium discoideum cytokinesis mutant. *J. Cell Biol.* **150**, 823–838. doi:10.1083/jcb.150.4.823
- Salvioli, S., Monti, D., Lanzarini, C., Conte, M., Pirazzini, C., Bacalini, M. G., Garagnani, P., Giuliani, C., Fontanesi, E., Ostan, R. et al.** (2013). Immune system, cell senescence, aging and longevity—inflam-aging reappraised. *Curr. Pharm. Des.* **19**, 1675–1679. doi:10.2174/138161213805219531
- Seminario-Vidal, L., Okada, S. F., Sesma, J. I., Kreda, S. M., van Heusden, C. A., Zhu, Y., Jones, L. C., O'Neal, W. K., Penuela, S., Laird, D. W. et al.** (2011). Rho signaling regulates pannexin 1-mediated ATP release from airway epithelia. *J. Biol. Chem.* **286**, 26277–26286. doi:10.1074/jbc.M111.260562
- Seo, J. B., Riopel, M., Cabrales, P., Huh, J. Y., Bandyopadhyay, G. K., Andreyev, A. Y., Murphy, A. N., Beeman, S. C., Smith, G. I., Klein, S. et al.** (2019). Knockdown of Ant2 Reduces Adipocyte Hypoxia And Improves Insulin Resistance in Obesity. *Nat Metab* **1**, 86–97. doi:10.1038/s42255-018-0003-x
- Simet, S. M., Sisson, J. H., Pavlik, J. A., Devasure, J. M., Boyer, C., Liu, X., Kawasaki, S., Sharp, J. G., Rennard, S. I. and Wyatt, T. A.** (2010). Long-term cigarette smoke exposure in a mouse model of ciliated epithelial cell function. *Am. J. Respir. Cell Mol. Biol.* **43**, 635–640. doi:10.1165/rcmb.2009-0297OC
- Sisson, J. H., Stoner, J. A., Ammons, B. A. and Wyatt, T. A.** (2003). All-digital image capture and whole-field analysis of ciliary beat frequency. *J. Microsc.* **211**, 103–111. doi:10.1046/j.1365-2818.2003.01209.x
- Tilley, A. E., Harvey, B.-G., Heguy, A., Hackett, N. R., Wang, R., O'Connor, T. P. and Crystal, R. G.** (2009). Down-regulation of the notch pathway in human airway epithelium in association with smoking and chronic obstructive pulmonary disease. *Am. J. Respir. Crit. Care Med.* **179**, 457–466. doi:10.1164/rccm.200705-795OC
- Vestbo, J., Hurd, S. S., Agustí, A. G., Jones, P. W., Vogelmeier, C., Anzueto, A., Barnes, P. J., Fabbri, L. M., Martinez, F. J., Nishimura, M. et al.** (2013). Global strategy for the diagnosis, management, and prevention of chronic obstructive pulmonary disease: GOLD executive summary. *Am. J. Respir. Crit. Care Med.* **187**, 347–365. doi:10.1164/rccm.201204-0596PP
- Wiegman, C. H., Michaeloudes, C., Haji, G., Narang, P., Clarke, C. J., Russell, K. E., Bao, W., Pavlidis, S., Barnes, P. J., Kanerva, J. et al.** (2015). Oxidative stress-induced mitochondrial dysfunction drives inflammation and airway smooth muscle remodeling in patients with chronic obstructive pulmonary disease. *J. Allergy Clin. Immunol.* **136**, 769–780. doi:10.1016/j.jaci.2015.01.046
- Winter, J., Klumpe, I., Heger, J., Rauch, U., Schultheiss, H.-P., Landmesser, U. and Dörner, A.** (2016). Adenine nucleotide translocase 1 overexpression protects cardiomyocytes against hypoxia via increased ERK1/2 and AKT activation. *Cell. Signal.* **28**, 152–159. doi:10.1016/j.cellsig.2015.11.002
- Yaghi, A., Zaman, A., Cox, G. and Dolovich, M. B.** (2012). Ciliary beating is depressed in nasal cilia from chronic obstructive pulmonary disease subjects. *Respir. Med.* **106**, 1139–1147. doi:10.1016/j.rmed.2012.04.001
- Zhou, Q., Kee, Y.-S., Poirier, C. C., Jelinek, C., Osborne, J., Divi, S., Surcel, A., Will, M. E., Eggert, U. S., Müller-Taubenberger, A. et al.** (2010). 14-3-3 coordinates microtubules, Rac, and myosin II to control cell mechanics and cytokinesis. *Curr. Biol.* **20**, 1881–1889. doi:10.1016/j.cub.2010.09.048

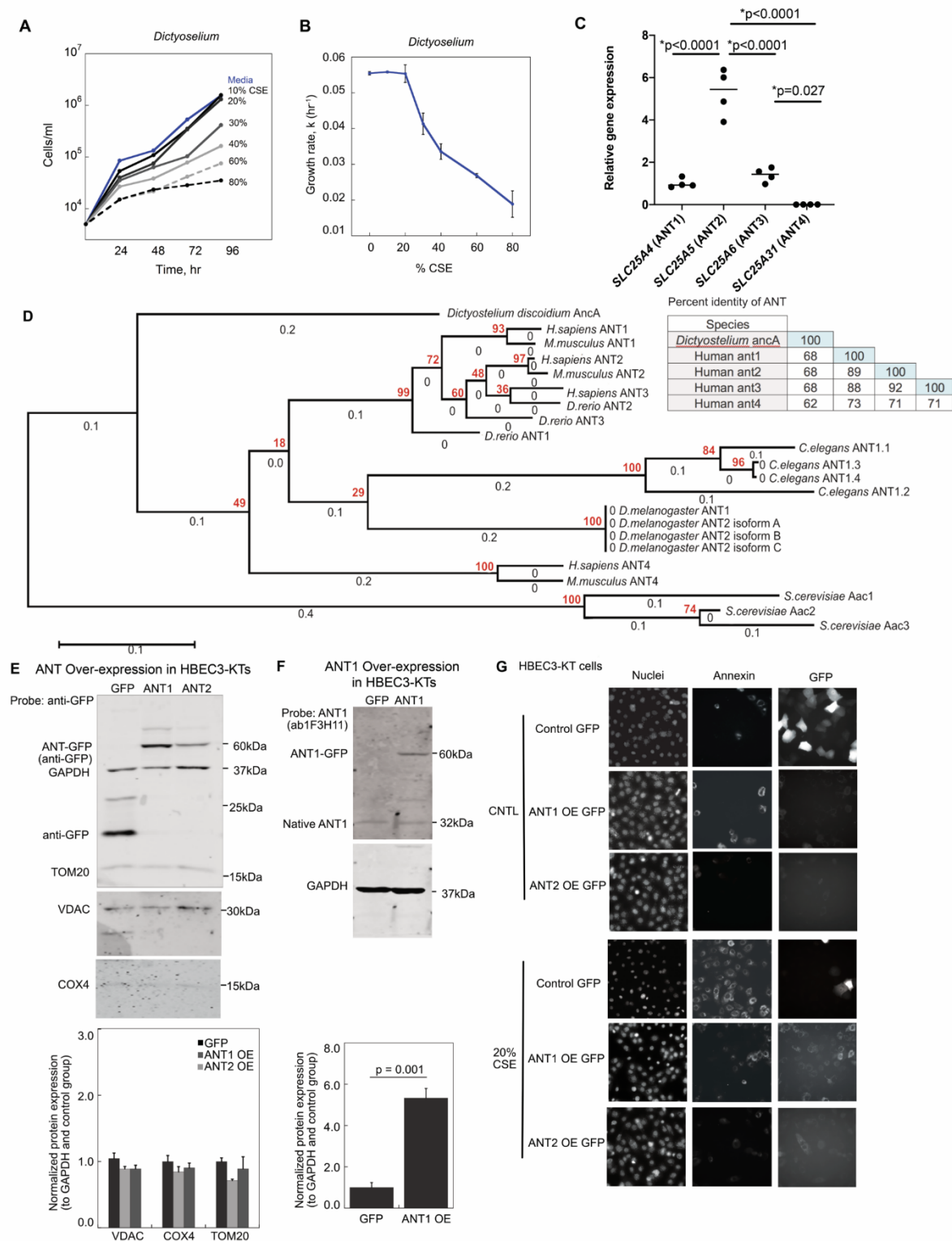


Fig. S1. ANT is a genetic protector of *Dictyostelium* and bronchial epithelial cells from cell death. **A)** *Dictyostelium* growth curves with 10-80% CSE. **B)** *Dictyostelium* growth curve to identify EC40 for 10-80% CSE. **C)** Relative gene expression of human *slc25a4* (ANT1), *slc25a5* (ANT2), *slc25a6* (ANT3) and *slc25a31* (ANT4) in primary differentiated normal human bronchial epithelial cells grown at air liquid interface. n = 4 inserts. Statistics by Mann Whitney; p-values are noted. **D)** Molecular phylogenetic tree analysis of adenine nucleotide translocase (AncA in *Dictyostelium* and ANT in humans) with bootstrap values. Percent identity for human ANT and *Dictyostelium* AncA, generated by Clustal2.1. **E)** Western analysis of adenoviral overexpression, OE (control GFP, ANT1-GFP and ANT2-GFP) in HBEC3-KTs evaluating for GFP, mitochondrial TOM20, VDAC, COX4 and GAPDH. **F)** ANT1 western analysis for ANT1 overexpression. **G)** Representative images of HBEC3-KTs depicting total nuclei (Draq5), apoptosis (Annexin V) and GFP (adenovirus infection).

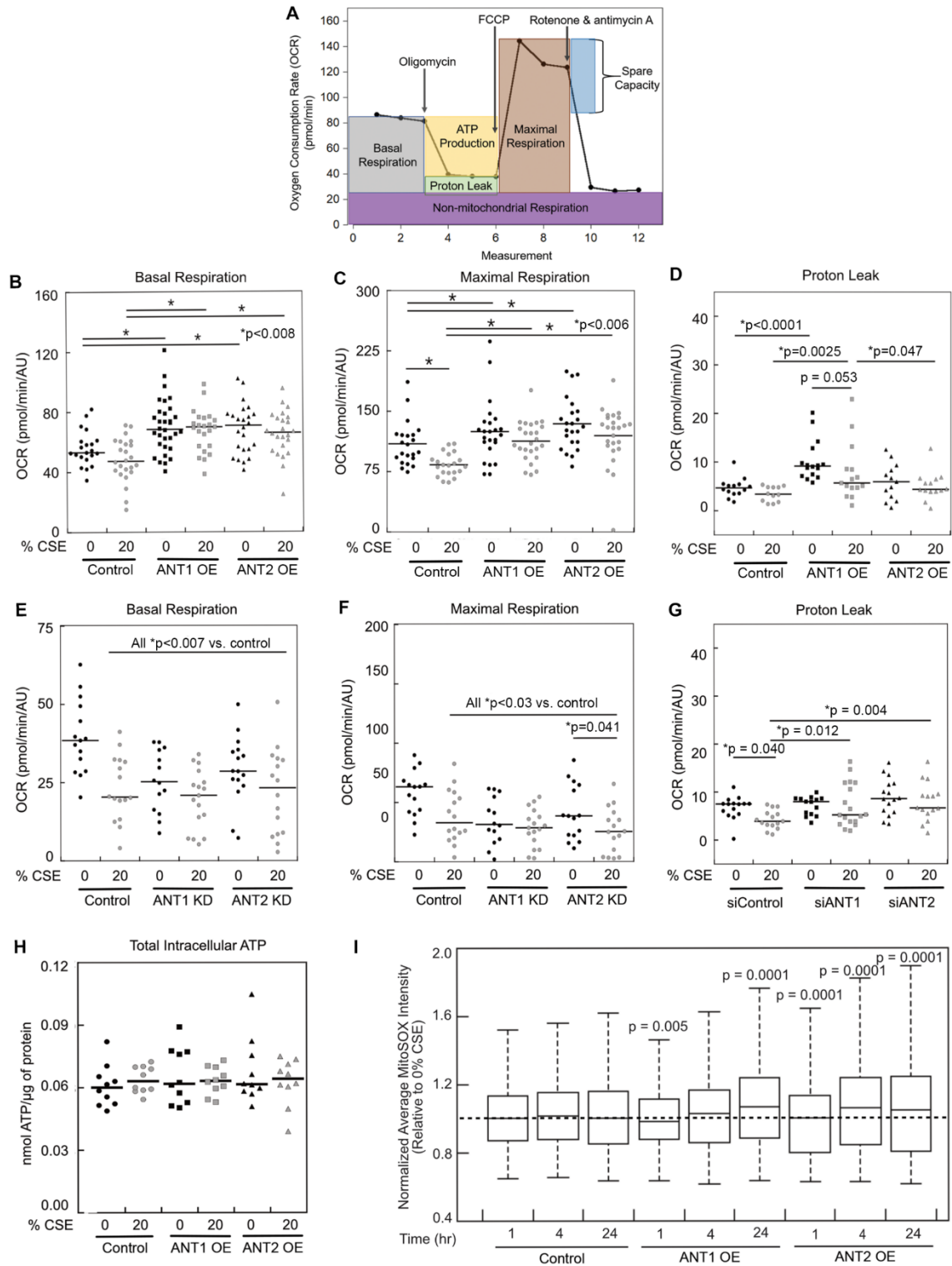


Fig. S2. Alterations in mitochondrial reactive oxygen species and metabolism due to ANT. Cellular metabolism by the Seahorse Mitostress assay. **A)** Example diagram of oxygen consumption rate (OCR) analysis before and after complex-specific inhibitors. Cellular metabolism was assessed by oxygen consumption rate in HBEC3-KT cells, with ANT1 or ANT2 adenoviral overexpression (**B, C, D**) or siRNA suppression (**E, F, G**). **B)** Basal OCR with ANT overexpression, **C)** Maximal OCR with ANT overexpression, **D)** Proton leak with ANT overexpression, **E)** Basal OCR ANT suppression, **F)** Maximal OCR with ANT suppression, **G)** Proton leak with ANT suppression, median bars are provided; n = 15-26 wells from 3 separate experiments. **H)** Measurements of total intracellular ATP in HBEC3-KTs with ANT1 or ANT2 overexpression $\pm 20\%$ CSE, yielding a total intracellular [ATP] of 8 mM for HBEC3-KT cells. Median bars shown; n = 10 wells per group from 5 separate experiments. **I)** Boxplot showing mitochondrial superoxide production (MitoSox) in HBEC3-KTs after CSE with ANT overexpression. Horizontal dotted line represents the median for the 1 hr control group. Boxplots show the median with the box delineating the 1st and 3rd quartiles. The whiskers represent 1.5*IQR (interquartile range). Statistics performed by Kruskal-Wallis and two-tailed Mann-Whitney U tests. P-values represent differences from Control at each respective time point. n = 2800-4500 cells per group.

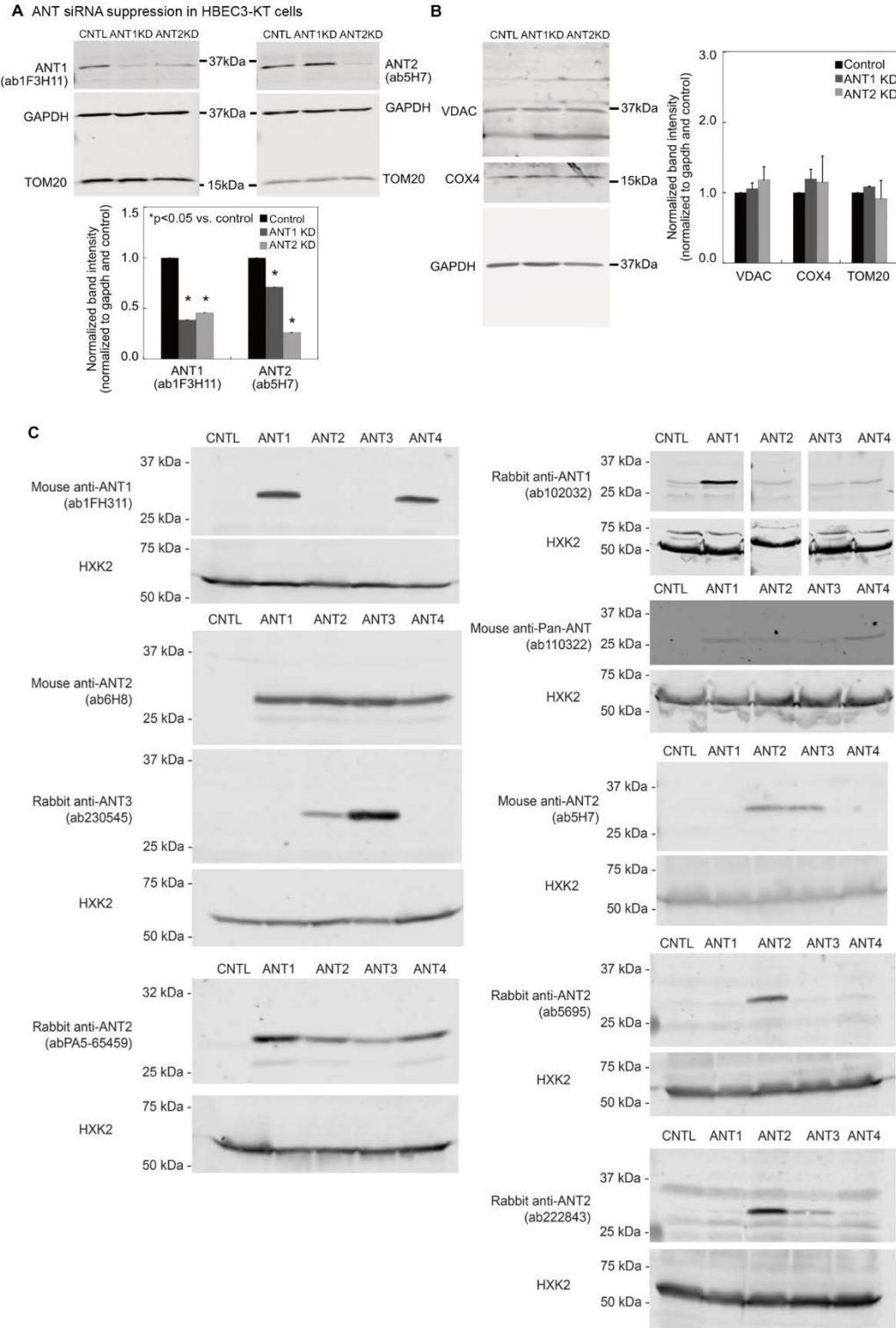


Fig. S3. Western blot analysis of ANT knockdown and antibody specificity. **A)** Western analysis of ANT siRNA suppression (knockdown, KD) probed for ANT1 (ab1F3H11), ANT2 (ab5H7), GAPDH and TOM20. Statistical analysis by ANOVA with Fisher's LSD posttest; $*p < 0.05$. **B)** Western analysis of ANT siRNA suppression probed for mitochondrial proteins VDAC and COX4. A bar graph summarizes the relative amounts of each protein across samples. Values in panels **A** and **B** are for $n = 3$ per group with band intensity quantification normalized to GAPDH. **C)** Antibody specificity was determined for rabbit and mouse anti-ANT antibodies utilizing yeast strains with expression of the individual human ANT paralogs, ANT1-4. Hexokinase-2 was used as the loading control.

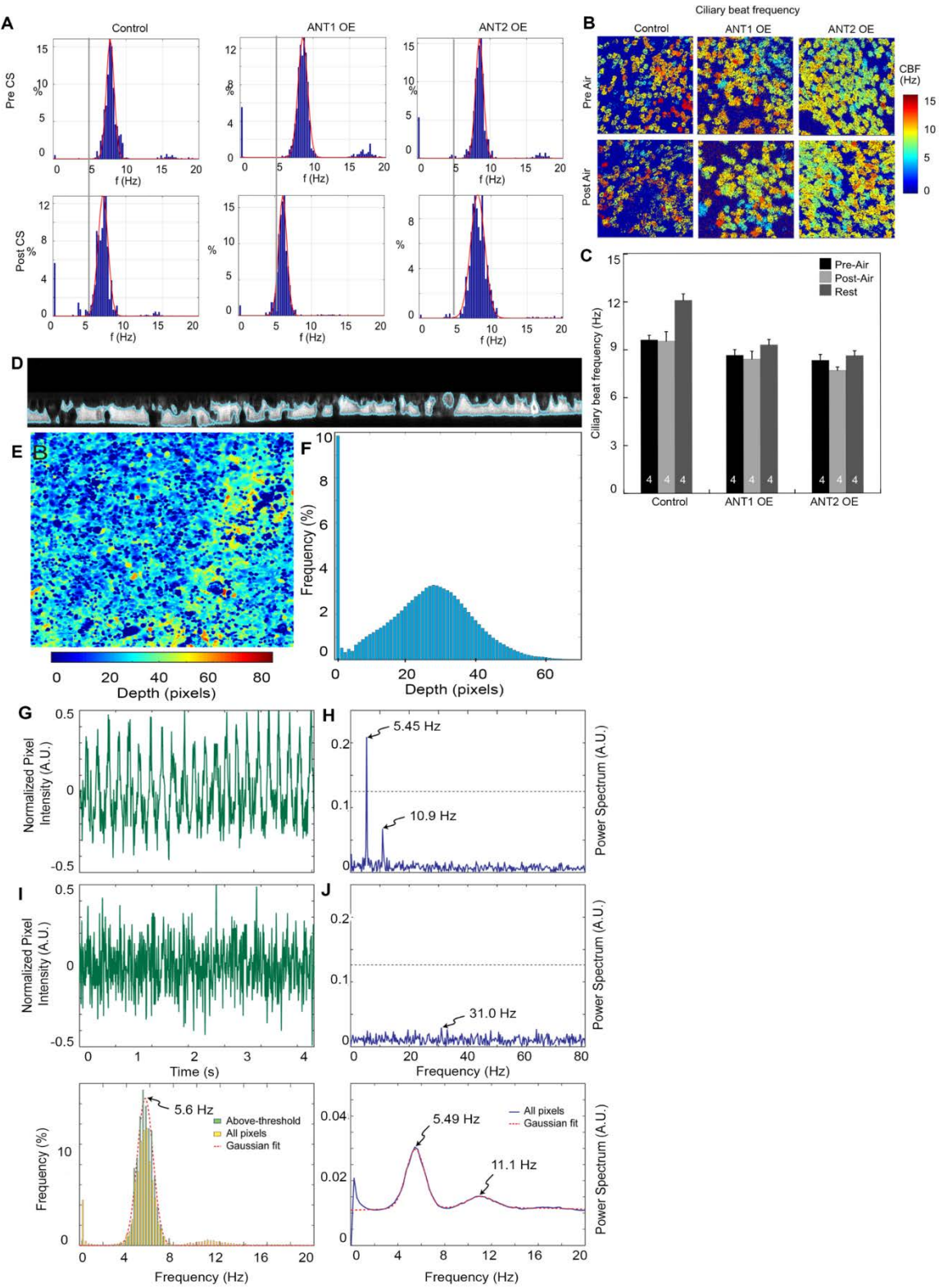


Fig. S4. Ciliary beat frequency analysis and ASL/CBF Methods **A)** CBF histograms from CS-treated NHBE cells. **B)** CBF heat maps and **C)** CBF data for air-treated NHBE cells. Data show mean \pm SEM and the “n” depicted on the bars equals the # of individual ALI inserts. Experiments are a compilation of insert data from 2-4 different days. Statistical analysis by ANOVA with Fisher’s LSD posttest with $p < 0.05$ as significant. **Method for airway surface liquid (ASL) thickness.** **D)** Sample of an (x, z) cross-section showing the original image and the segmented regions. **E)** Heat map showing thickness across the sample. **F)** Histogram showing the pixel thicknesses across the region in panel B. **Method for computing ciliary beating frequency (CBF).** **G)** Data from two different pixels from a video was normalized so that it ranged from 0 to 1 and then readjusted to have zero mean. **H)** These time courses were used to compute the single-sided spectrum for each pixel, shown for the two pixels in panel A. To consider only pixels with considerable oscillatory behavior (e.g. top pixel in panel A, but not bottom), a threshold of 0.125 A.U. was set for the maximum power, shown by the dotted lines. **I)** The frequency where the maximal power was observed for each of the pixels was computed, and this plotted as a histogram. Shown are the histograms for all pixels, and only for those with maximum pixel intensity above the threshold. The latter was fit to a single Gaussian, shown by the dotted line. This was used to determine the average beating frequency for the sample. **J)** As an alternative check, the power spectrum over all pixels was computed, and fit by a Gaussian mixture model (red dotted line).

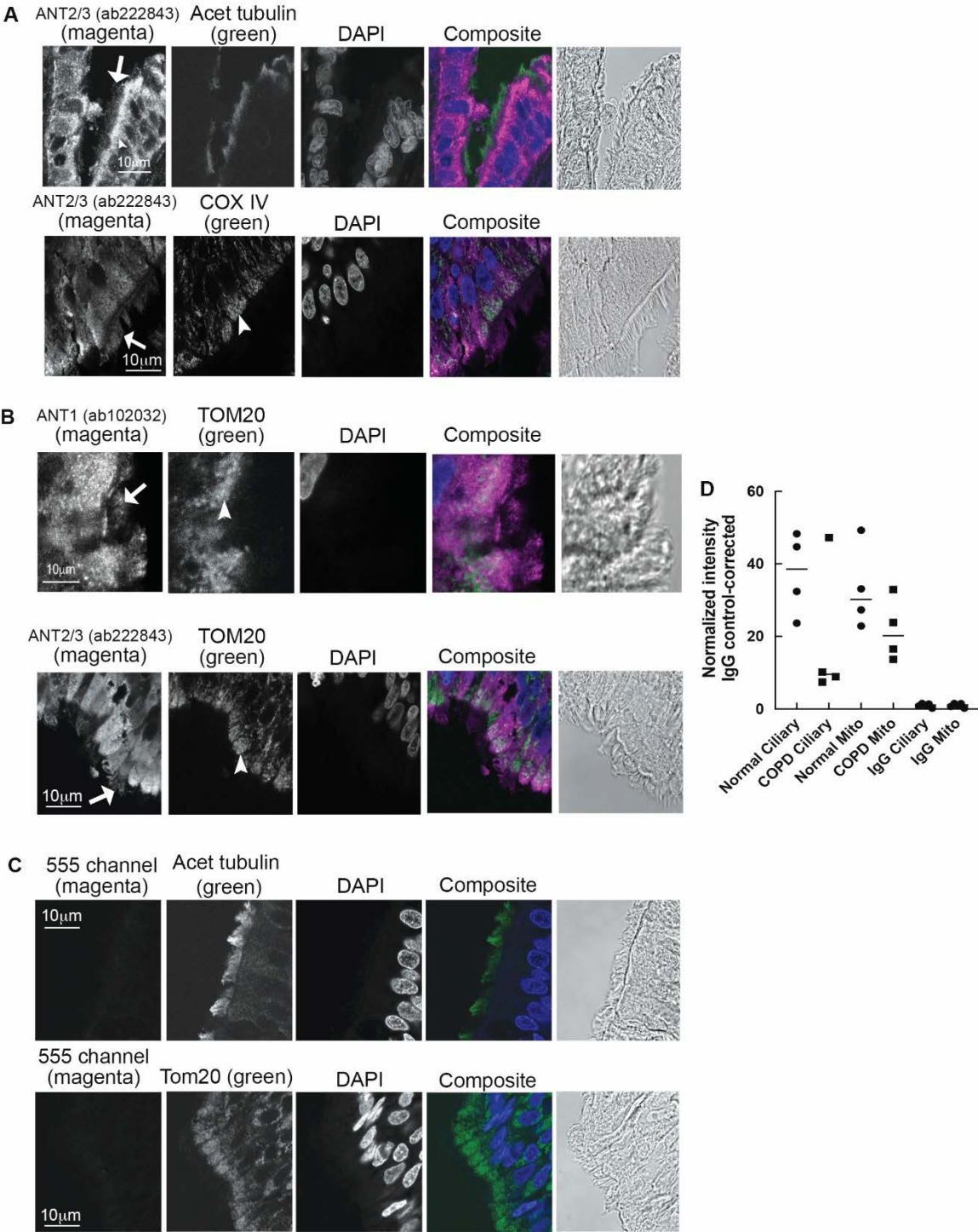


Fig. S5. ANT localization in the human airway epithelium. **A)** Human lung tissue with immunofluorescence for ANT2/3 (ab222843, magenta) with colocalization of ANT with acetylated α -tubulin and cytochrome c oxidase, COX IV (green). The full arrow identifies the layer of cilia and arrowhead identifies the mitochondrial layer. Representative images from 1 patient. **B)** Human lung tissue with immunofluorescence for ANT1 (ab102032, magenta) or ANT2/3 (ab222843, magenta) with colocalization of ANT with the mitochondrial protein, TOM20 (green). The full arrow identifies the layer of cilia and arrowhead identifies the mitochondrial layer. Representative images from 2 patient tissues. **C)** Control staining of human airway tissue for acetylated α -tubulin or TOM20 (green) without evidence of bleed through into the 555 channel (magenta). **D)** Quantification of ANT staining in normal and COPD lung tissue, assessing ciliary and mitochondrial layers of staining. Corrected for background and normalized to non-immune IgG staining controls. Medians are shown. Statistical analysis using a Mann Whitney test.

A Human lung tissue

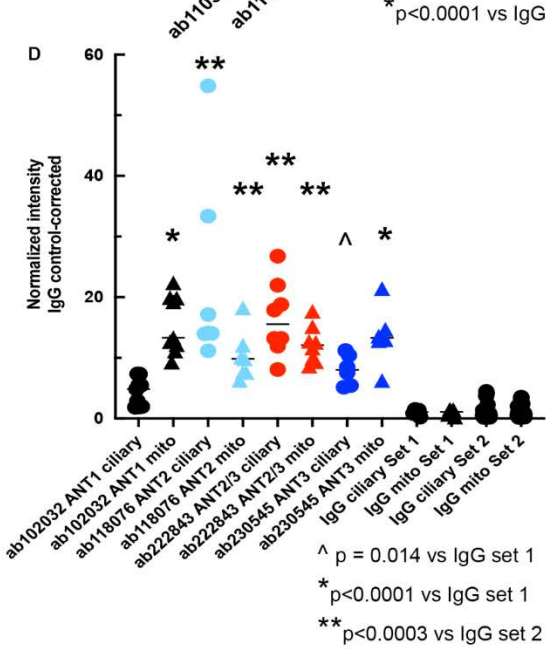
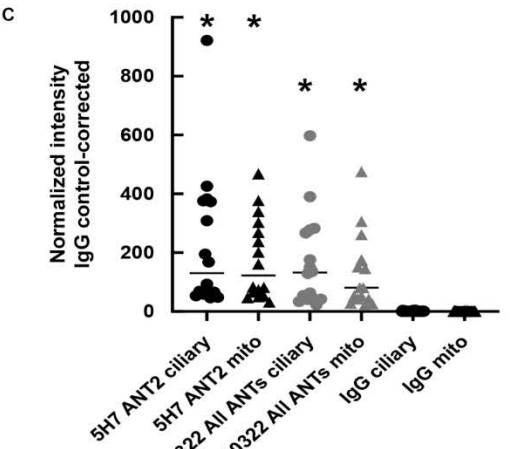
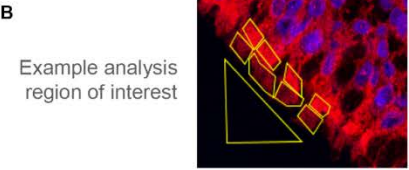
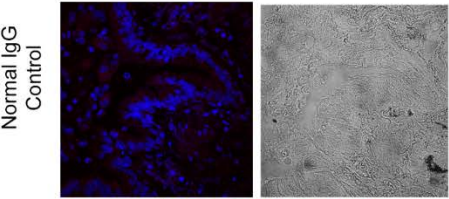
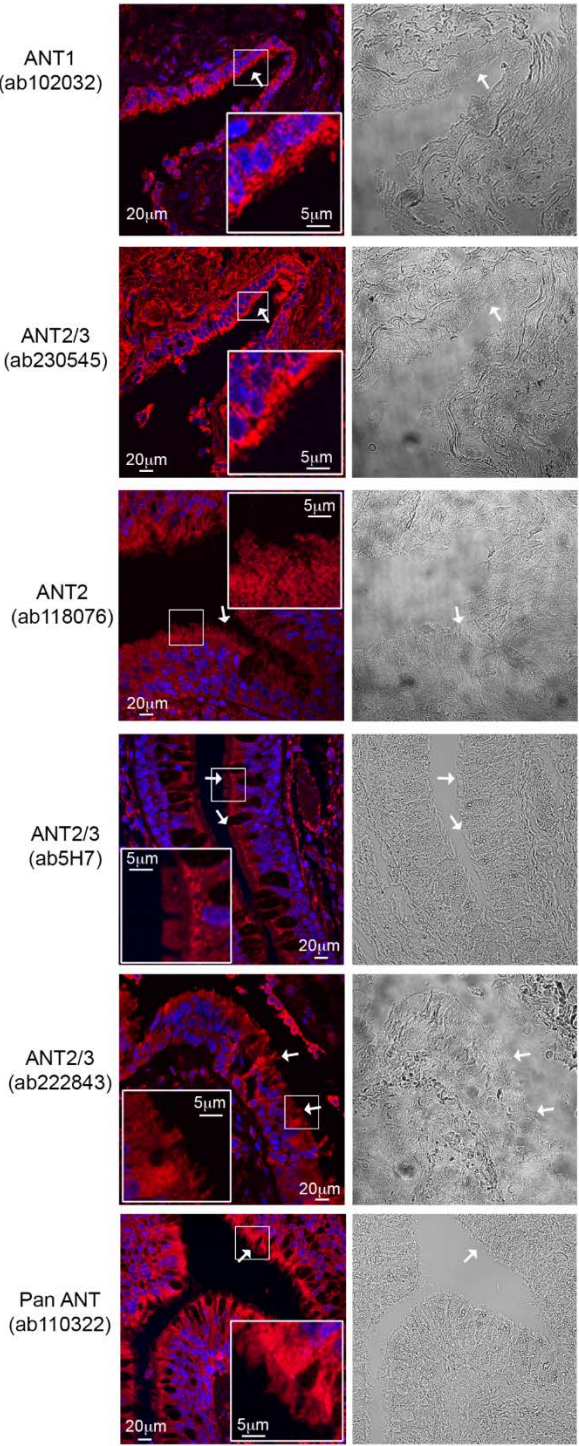


Fig. S6. ANT antibody panel in the ciliated airway epithelium of normal human lung tissue. **A)** ANT antibodies were tested on normal human lung tissue (formalin fixed, paraffin embedded) for cellular localization. Associated DIC images are provided to allow identification of the apical layer of cilia. ANT staining at the ciliary plasma membrane is noted with the long white arrow while mitochondrial ANT is noted with the short arrow. Enlarged insets are included, scale bar 5 μm . **B)** Example of analysis completed on the apical cilia layer versus subcellular mitochondrial layer. The large triangle represents background analysis. **C)** Quantification of ciliary layer (●) versus mitochondrial layer (▲) for each antibody analyzed, ANT2 (ab5H7) and All ANTs (Pan-ANT ab110322). Each set of staining was completed with non-immune IgG staining controls, which served as the comparison. $n = 3$ patient samples. Medians are shown. P-values from ANOVA with Fisher's LSD post hoc test. One patient sample was noted to have higher staining intensity as evident in the data set. **D)** Quantification of ciliary versus mitochondrial layer for each antibody analyzed, ANT1 (ab102032), ANT2 (ab118076), ANT2/3 (ab222843) and ANT3 (ab230545). Each set of staining was completed with non-immune IgG staining controls which served as the normalization. $n = 3\text{-}5$ patient samples. Medians are shown. P-values from ANOVA with Fisher's LSD post hoc test.

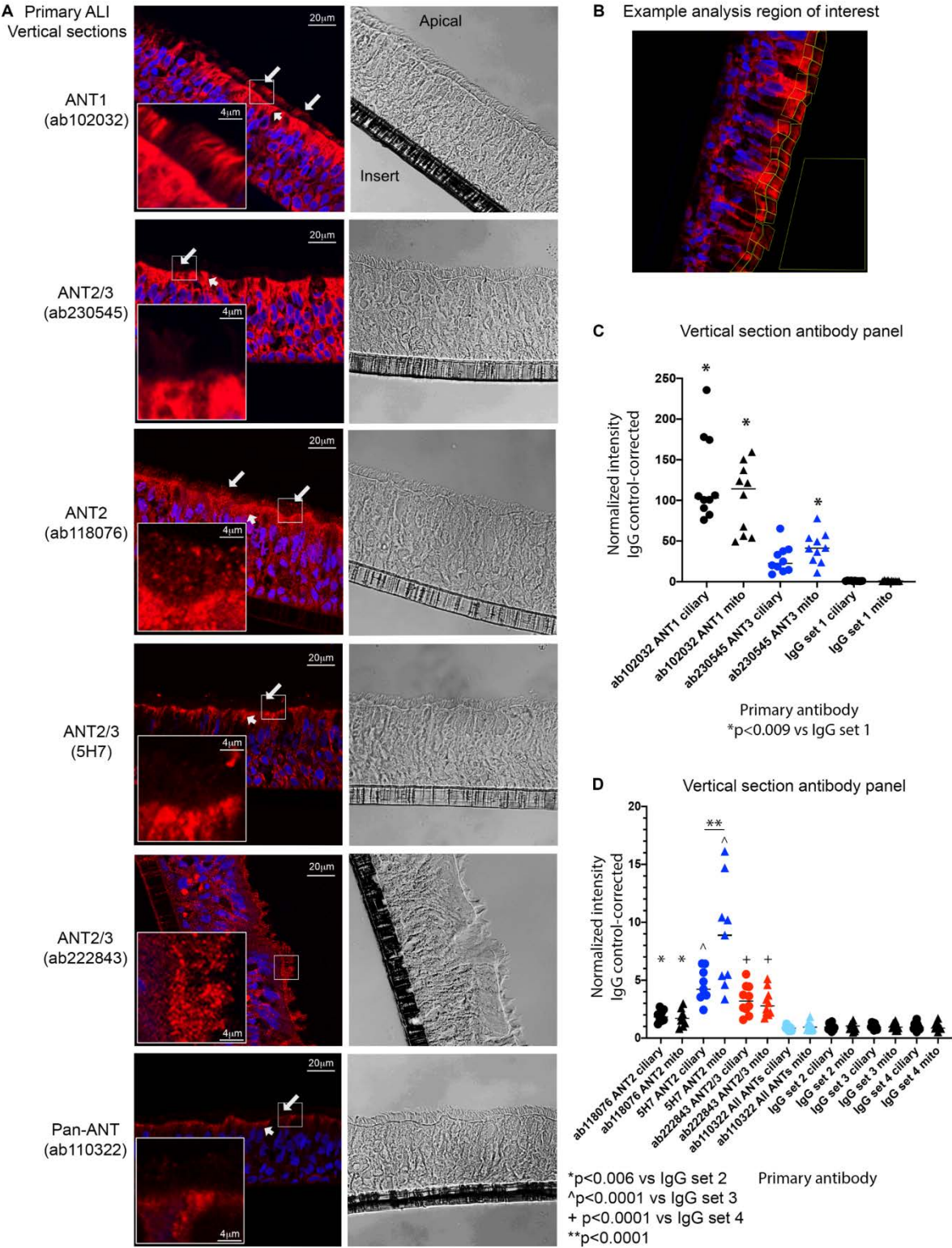


Fig. S7. ANT antibody panel in ciliated human bronchial epithelial cells grown at air liquid interface. **A)** ANT antibodies were tested on primary normal human bronchial epithelial cells differentiated at air liquid interface on cell culture inserts. Frozen sections were cut of the cells grown on inserts and subsequently stained for ANT cellular localization. Associated DIC images are shown to allow identification of the apical layer of cilia. ANT staining at the ciliary plasma membrane is noted with the long white arrow while mitochondrial ANT is noted with the short arrow. Enlarged insets are included, scale bar 4 μm . **B)** Example of analysis completed on the apical cilia layer versus subcellular mitochondrial layer with an area for background analysis. Please see the immunofluorescence staining section of the methods for quantification methodology. **C, D)** Quantification of ciliary layer (●) versus mitochondrial layer (▲) for each antibody analyzed. Each set of staining was completed with non-immune IgG staining controls which served as the normalization. Represents cells from $n = 3\text{-}5$ patients. Median bars are shown. Statistics by ANOVA with Fisher's LSD posttest, p -values are noted in the figure.

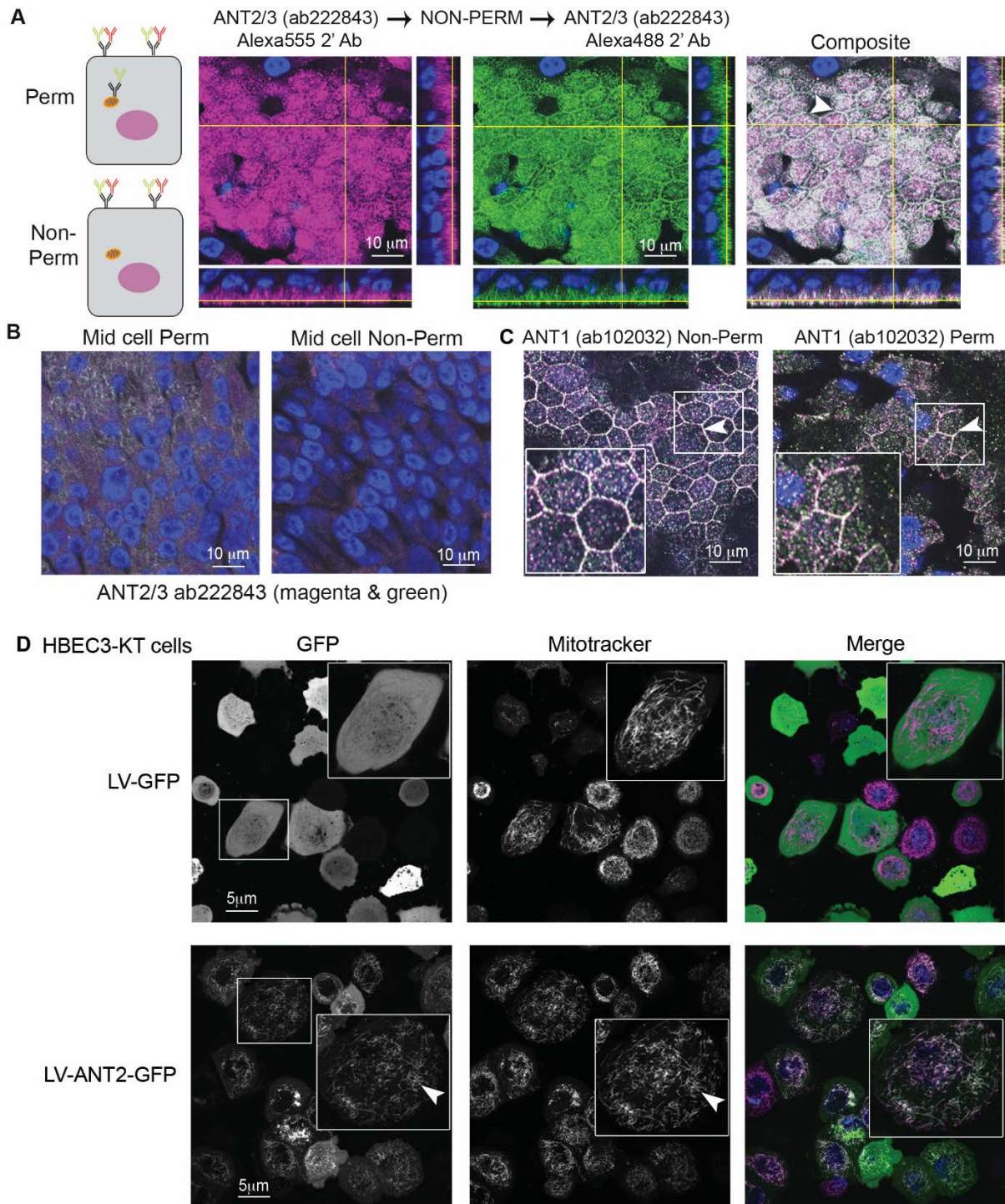
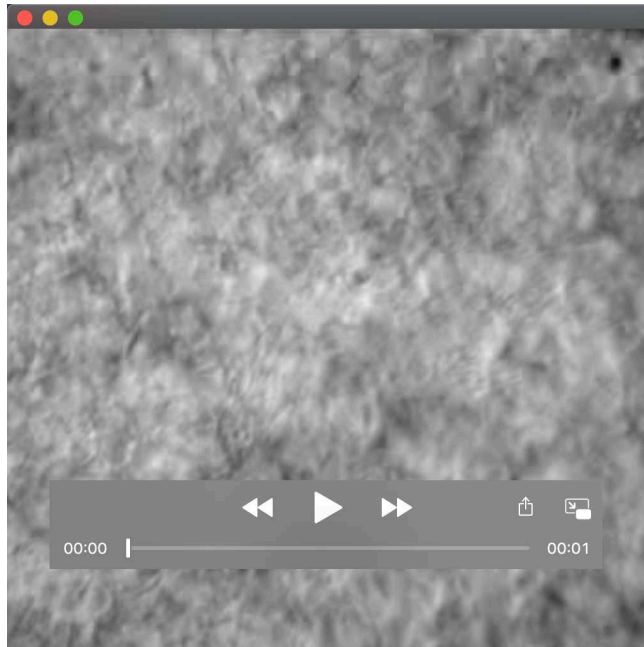


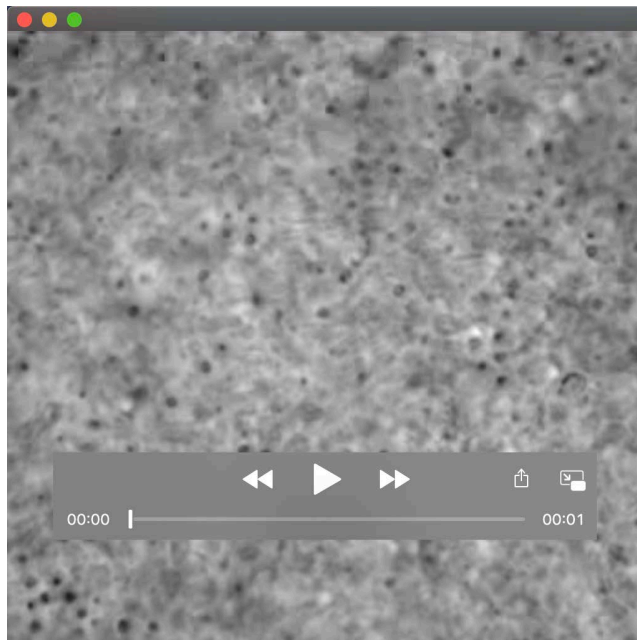
Fig. S8. ANT plasma membrane localization in primary air-liquid interface cultures. A) A population of ANT2/3 localizes to the plasma membrane in NHBE cells. NHBE cells were stained for ANT2/3 (without prior permeabilization) followed by secondary antibody Alexa 555 (magenta). Without permeabilization (non-perm), samples were subsequently stained again with anti-ANT2/3 followed by a secondary antibody Alexa 488 (green). Colocalization is evident at the cell borders and surface (white). Scale bar, 10 μ m. n = 3 inserts. **B)** A representative confocal image from a cross-section through the middle of permeabilized and non-permeabilized cells stained with ab222843 (as in panel E), revealing intracellular staining of ANT in the permeabilized, but not non-permeabilized, ALI cells. **C)** ANT1 localizes to the plasma membrane in NHBE cells. In the left panel, NHBE cells were stained for ANT1 using ab102032 (secondary antibody Alexa 555, magenta) without permeabilization and subsequently stained with ab102032 (secondary antibody Alexa 488, green). In the right panel, NHBEs were stained with ab102032 (secondary Alexa 555, magenta), permeabilized (perm) and subsequently stained with ab102032 (secondary Alexa 488, green). Colocalization is depicted as white. Scale bar, 10 μ m. n = 2 inserts. The inset provides a close-up view. **D)** ANT2-GFP, but not GFP, colocalizes with mitochondria in HBEC3-KT cells (arrowhead). Lentiviral ANT2-GFP or GFP control was overexpressed in HBEC3-KT cells. Cells were stained with mitotracker (magenta) and imaged with confocal microscopy. Scale bar, 5 μ m.



Movie 1.

Kliment et al. Suppl Video 1_CTRL pre-CS

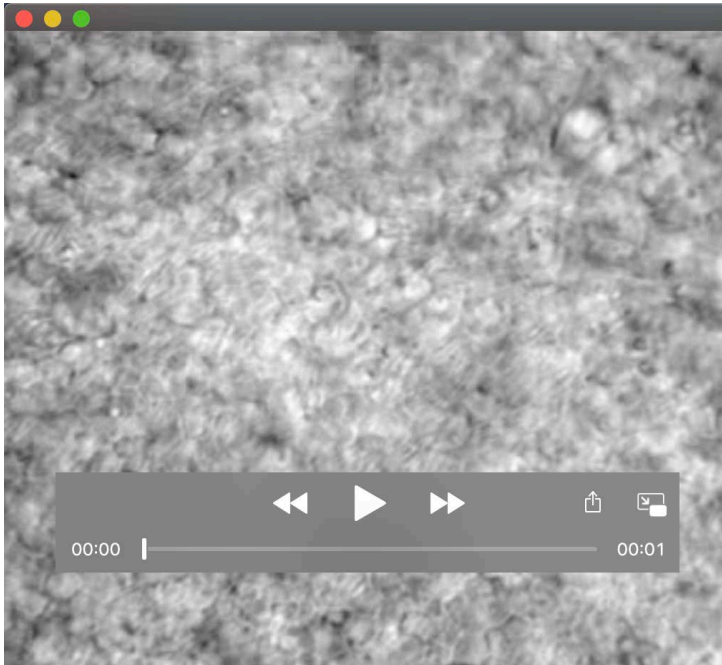
Ciliary beat frequency (CBF) in NHBE cells (control adenovirus) before exposure to CS.



Movie 2.

Kliment et al. Suppl Video 2_CTRL post-CS

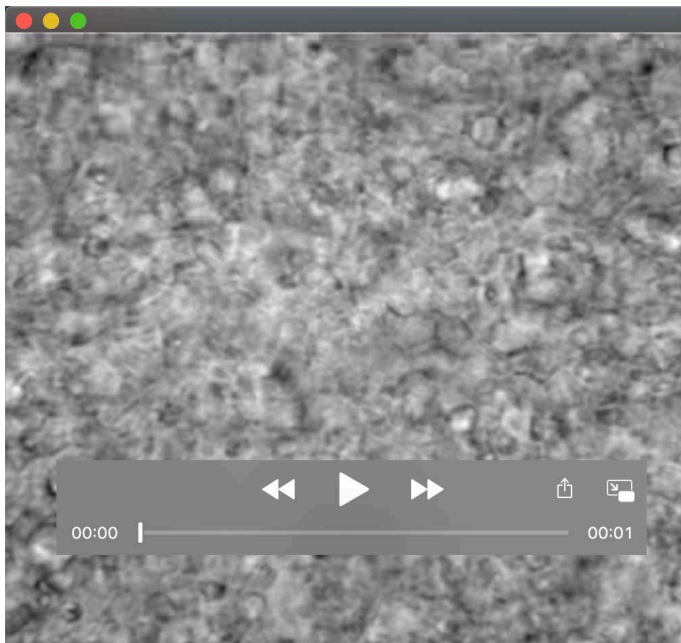
CBF in NHBE cells (control adenovirus) 30 min after exposure to CS, showing a slowing of CBF.



Movie 3.

Kliment et al. Suppl Video 3_ANT1 pre-CS

CBF in NHBE cells (ANT1-GFP adenovirus) before exposure to CS.



Movie 4.

Kliment et al. Suppl Video 4_ANT1 post-CS

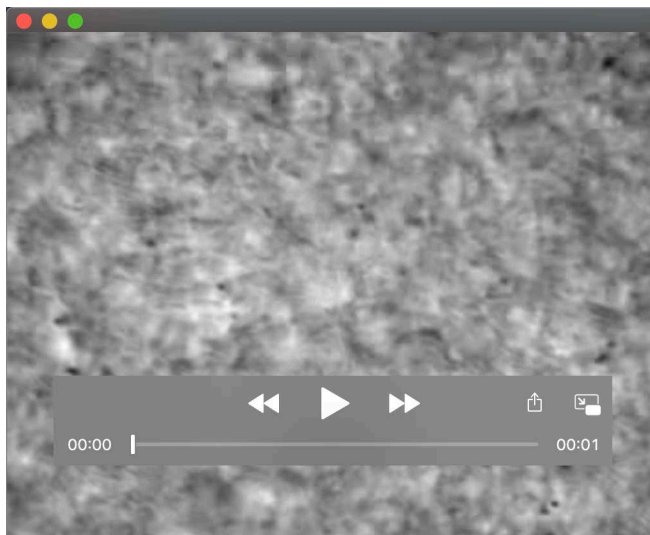
CBF in NHBE cells (ANT1-GFP adenovirus) 30 min after exposure to CS, showing a slowing of CBF.



Movie 5.

Kliment et al. Suppl Video 5_ ANT2 pre-CS

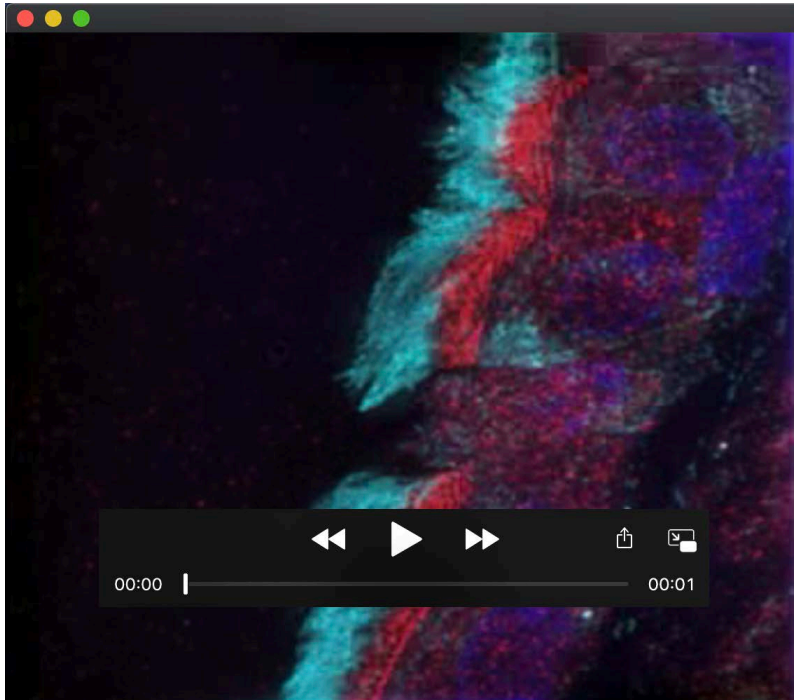
CBF in NHBE cells (ANT2-GFP adenovirus) before exposure to CS.



Movie 6.

Kliment et al. Suppl Video 6_ ANT2 post-CS

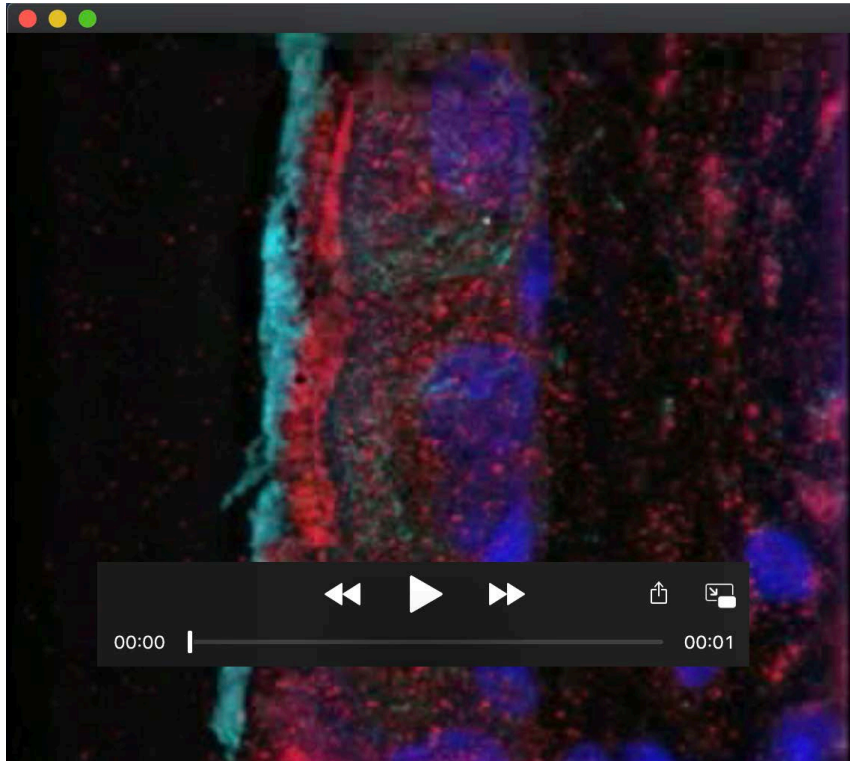
CBF in NHBE cells (ANT2-GFP adenovirus) 30 min after exposure to CS, showing preservation of CBF.



Movie 7.

Kliment et al. Suppl Video 7_Air treated mouse lung

SIM imaging of air-treated mouse lung stained for ANT1 (red, Rabbit anti-human ANT1 antibody, ab102032), tubulin (light blue) and nuclei (dark blue). ANT1 localizes to the plasma membrane surface in a linear pattern on the apical cell surface and to cilia in a striated pattern. ANT also localizes to mitochondria in the cell body.



Movie 8.

Kliment et al. Suppl Video 8_Smoke treated mouse lung

SIM imaging of cigarette smoke-treated mouse lung stained for ANT1 (red, rabbit anti-human ANT1, ab102032), tubulin (light blue) and nuclei (dark blue). ANT1 localizes to the plasma membrane surface in a linear pattern on the apical cell surface and to cilia with loss of patterning. ANT also localizes to mitochondria in the cell body.

Table S1. Key Resources.

| REAGENT or RESOURCE | SOURCE | IDENTIFIER |
|---|---|--|
| Antibodies | | |
| Human ANT1 (mouse) – 1:500 Western | Lu et al (Lu et al., 2017) | #ab1F3H11 |
| Human ANT2 (mouse) - 1:500 Western; 1:100 IHC | Panneels et al (Panneels et al., 2003) | #ab5H7 |
| Human acetylated α -tubulin Rabbit, 1:2000 Mouse, 1:2000 | Cell Signaling Invitrogen | #5335T #32-2700 |
| Human TOM20 (1:1000, rabbit monoclonal) – Western and IHC | Abcam Cell Signaling | #ab186734 #42406S |
| Human GAPDH (rabbit) – Western 1:1000 | Life Technologies | #A6455 |
| ANT1 (rabbit polyclonal) – IHC 1:1000 | Abcam | #ab102032 |
| Human Pan ANT (mouse monoclonal) - IHC (1:100) | Abcam | #ab110322 |
| Human ANT2 (mouse monoclonal) – IHC, 1:100 | Abcam | #ab118076 |
| Human ANT2 – IHC, 1:1000 | Abcam | #ab222843 |
| Human ANT2/3 – IHC, 1:100 | Abcam | #ab230545 |
| GFP, (chicken polyclonal) – IHC 1:1000 | Aves Labs Inc | #GFP-1010 |
| Goat anti-mouse or rabbit Alexa 488, 555 and 647 | Molecular Probes | 488 – mouse R37120; rabbit R37116, Chicken A11039 555 – mouse A21424; rabbit A21429 647 – mouse A21236; rabbit A21245 |
| Human COX4-Alexa Fluor 488 conjugate – IHC 1:200 | Cell Signaling | #4853S |
| Mammalian COX4 (rabbit mAb) - Western 1:1000 | Cell Signaling | #4850 |
| Mammalian VDAC (rabbit pAb; raised against VDAC-1, but recognizes all VDACs) - Western 1:1000 | Cell Signaling | #4866 |
| Yeast HXK2 (rabbit pAb) – Western 1:50,000 | Gift from Robert Jensen, Johns Hopkins University, Baltimore, MD, USA | |
| Bacterial, Yeast and Virus Strains | | |
| <i>E. coli</i> BL-21 DE3 cells | ThermoFisher | #C600003 |
| <i>E. coli</i> STBL2 | ThermoFisher | #10268019 |
| Yeast expressing human ANT1-4 | Steven Claypool, Johns Hopkins | Δ aac[EV], Δ aac[ANT1], Δ aac[ANT2], Δ aac[ANT3], Δ aac[ANT4] |

| | | |
|---|--|---|
| Adenovirus constructs – GFP-tagged | Vector Biolabs (Malvern, PA) | control eGFP (#1060) ANT1-GFP (Ad-h- <i>slc25a4</i> /eGFP, GenBank BC008664.1) ANT2-GFP(Ad-h- <i>slc25a5</i> /eGFP, GenBank BC056160.1) |
| Lentiviral constructs – GFP-tagged | Vector Builder Inc | control GFP (LVM (VB160109-10005) and ANT2-gfp (Cat#: LVS(VB190613-1074dha)-C) |
| Biological Samples | | |
| Mouse olfactory and upper respiratory tissues | Randal Reed, Johns Hopkins University | Mouse |
| Lung Genome Research Consortium (LGRC), GWAS analysis of whole lung tissue samples | Frank Sciurba, University of Pittsburgh | - |
| Human lung tissue for real-time PCR gene expression analysis (Control and COPD lung) | The Airway Cell and Tissue Core at the University of Pittsburgh | Human lung |
| Human lung tissue (Immunohistochemistry) | Tissue Core at the University of Pittsburgh and National Heart, Lung, and Blood Institute's Lung Tissue Research Consortium database | Control and COPD lung tissue |
| Chemicals, Peptides, and Recombinant Proteins | | |
| Research grade cigarettes (3R4F) | Tobacco Health Research Institute, University of Kentucky | Type: 3R4F |
| Critical Commercial Assays/Equipment | | |
| One-step VERSO SYBR green PCR kit | Thermo Fisher Scientific | #AB4104A |
| Vitrocell cigarette smoke exposure system | Vitrocell (Germany) | VC1 |
| Luciferin-luciferase bioluminescence ATP Determination Kit | ThermoFisher | #A22066 |
| Cyquant Assay | Molecular Probes, ThermoFisher | #C35011 |
| Apoptosis & Healthy Cells Quantitation Kit Plus | Biotium, Inc | #30066 |
| Mitostress Test Kit (96-well format) Seahorse XF base medium Seahorse Calibrant Solution Seahorse XFe96 FluxPak (culture/assay plates) | Agilent Seahorse | #103015-100 #102353-100 #100840-000 #102416-100 |
| Deposited Data | | |

| | | |
|--|---|---|
| Geo Omnibus Publicly available data GDS2486 | Previously published (Harvey et al., 2007; Tilley et al., 2009) | #GDS2486 |
| Experimental Models: Cell Lines, Primary cells | | |
| Primary Normal Human bronchial epithelial cells (vial) | Lonza (Switzerland) | CC-2540S |
| Primary Normal Human bronchial epithelial cells (grown directly from human lung, unfrozen) | University of Pittsburgh Airway and Tissue Core | |
| Primary Normal Human bronchial epithelial cells (vial) | MatTek (MA, USA) | NHBE-CRY |
| Primary Normal Human bronchial epithelial cells (pre-cultured on transwell inserts) | Epithelix (France) | EP01-MD |
| HBEC3-KT, Immortalized human bronchial epithelial cell line | John Minna | HBEC3-KT |
| Experimental Models: Organisms/Strains | | |
| <i>Dictyostelium discoideum</i> | Douglas Robinson, Johns Hopkins University | Ax3(Rep ORF+7-3) |
| Mouse - C57Bl/6J mice for smoke exposure model | Jackson Labs | #000664 |
| ANT1 null mice | Douglas Wallace, CHOP, Philadelphia, PA | |
| Oligonucleotides | | |
| Primer sets: Mouse <i>slc25a4</i> /ANT1 Mouse <i>slc25a5</i> /ANT2 | Sigma KiQ primer sets | #M_Slc25a4_1 #M_Slc25a5_1 |
| human <i>slc25a4</i> /ANT1 PCR primers | IDT (synthesis) | forward 5'- TGG ATG ATT GCC CAG AGT GT and reverse 5'- GGC TCC TTC GTC TTT TGC AA-3'; |
| Human <i>slc25a5</i> /ANT2 PCR primers | IDT (synthesis) | forward 5'-GGC TTT AAC GTG TCT GTG CA-3' and reverse 5'-ATA GGA AGT CAA CCC GGC AA-3' |
| Human <i>slc25a6</i> /ANT3 PCR primers | IDT (synthesis) | forward 5'- ACG CCC TCC ATT CAC TCT C -3' and reverse 5'- GCT TGA CCC GCT CGA TCG -3' |
| Human <i>slc25a31</i> /ANT4 PCR primers | IDT (synthesis) | forward 5'- TTC CGC TTC CCT TCA TCG TA-3' and reverse 5'- GCC ACC GCT GTC TTG GAC-3' |
| <i>ACTB</i> (Beta-actin) | IDT (synthesis) | forward 5'-ATC CGC CGC CCG TCC-3' and reverse 5'- CGA TGG AGG GGA AGA CGG-3' |

| | | |
|---|---|--|
| <i>Dictyostelium AncA</i> | IDT (synthesis) | forward 5' – AAAAAAGTCGACATGTCTAA CCAAAAGAAAAACGACGTAT CTTCATTTG-3'; reverse 5'AAAAAAGCGGCCGCTTATT CAGAACCAACACCACC-3' |
| Recombinant DNA and siRNA | | |
| pLD1A15SN and GFP-pLD1A15SN | Douglas Robinson, Johns Hopkins University (Robinson and Spudich, 2000; Zhou et al., 2010) | plasmids |
| siRNA ON-TARGETplus smart pools | Dharmacon | ANT1 (<i>slc25a4</i> , #L-007485-00-0005), ANT2 (<i>slc25a5</i> , # L-007486-02-0005) non-targeting control pool #D-001810-10-05 |
| MatLab Scripts | | |
| Airway surface liquid (ASL) thickness analysis | Pablo Iglesias, Johns Hopkins University | Matlab (Mathworks, Natick, MA) |
| Ciliary beat frequency analysis (CBF) | Pablo Iglesias, Johns Hopkins University | Matlab |
| Other | | |
| 0.05% trypsin and trypsin neutralizing solution | ThermoFisher | #25300054; # CC-5002 |
| Carboxyatractyloside (CATR), Bongkreikic acid (BKA), and Apyrase | Sigma | CATR #C4992 BKA # 203671 Apyrase |
| Prolong Diamond Antifade Mounting Agent | Molecular Probes, ThermoFisher | #P36961 |
| RIPA cell lysis buffer with protease inhibitor cocktails I, II and III, RNase and aprotinin | Sigma | #R0278 # <u>P8340</u> #55674 # 10981532001 |
| Leibovitz L-15 buffered media | Gibco | # 11415064 |
| Keratinocyte serum free media | ThermoFisher | # 17005042 |
| BEGM media with Singlequot media supplement bullet kit | Lonza | CC-3170 |
| Bovine pituitary extract | AthenaES | #0414 |
| Transwell inserts, transparent 0.4- μ m pore PET | Falcon | #353090, 353190, 353095 |
| Bovine serum albumin | Sigma | A9647 |
| Retinoic acid | Sigma | R2625 |
| Epidermal growth factor | Sigma | E9644 |
| Type I collagen | Invitrogen | A1048301 |
| Trizol for total RNA isolation | Thermo Fisher, Grand Island, NY | #15596018 |

| | | |
|---|--------------------------------------|--------------|
| Reverse transcriptase | Applied Biosystems, Grand Island, NY | 4368814 |
| Sybr green master mix for real time PCR | Applied Biosystems | 4309155 |
| Texas Red Dextran, 10 kD | ThermoFisher | #D1817 |
| Fluorinert FC-70 | Millipore Sigma | #F9880 |
| Draq5 | Cell Signaling | #4084 |
| MitoSox Red | ThermoFisher | #M36008 |
| ecto-ATPase inhibitor ARL 67156 | Sigma | #A265 |
| Lipofectamine 2000 | Invitrogen | #11668019 |
| FM Medium | ForMedium, Norfolk, UK | FMM0103 |
| HL5 Medium | ForMedium | HLG0103 |
| Peptone and Yeast Extract | ForMedium | PEP04, YEA04 |
| Sodium pyruvate (used in Seahorse assay medium) | ThermoFisher | 11360070 |
| L-glutamine (used in Seahorse assay medium) | ThermoFisher | 25030081 |
| 45% Glucose (used in Seahorse assay medium) | Corning | 25-037-CI |